USING SMALL-ANGLE X-RAY SCATTERING TO INVESTIGATE THE COMPACTION BEHAVIOUR OF A GRANULATED CLAY.

Peter R Laity[1]*, Kofi Asare-Addo[2], Francis Sweeney[1], Enes Šupuk[2], Barbara R Conway[2]

1) Department of Materials Science and Engineering, University of Sheffield, Sir Robert Hadfield Building, Mappin Street, Sheffield, S1 3JD, UK

2) Department of Pharmacy, University of Huddersfield, Queensgate, Huddersfield UK. HD1 3DH

* indicates author for correspondence:

email: petelaity@aol.com

tel. (+44) 1484 316114

Email addresses of co-authors:

K.Asare-Addo@hud.ac.uk

f.sweeney@shef.ac.uk

E.Supuk@hud.ac.uk

B.R.Conway@hud.ac.uk

KEYWORDS:

Smectite; Compaction behaviour; Mechanical properties; Small-angle X-ray scattering (SAXS); Pharmaceutics.

ABSTRACT:

The compaction behaviour of a commercial granulated clay (magnesium aluminium smectite, gMgSm) was investigated using macroscopic pressure-density measurements, X-ray diffraction (XRD), scanning electron microscopy (SEM), X-ray microtomography (XμT) and small-angle X-ray scattering (SAXS). This material was studied as a potential compaction excipient for pharmaceutical tabletting, but also as a model system demonstrating the capabilities of SAXS for investigating compaction in other situations.

Bulk compaction measurements showed that the gMgSm was more difficult to compact than polymeric pharmaceutical excipients such as spheronised microcrystalline cellulose (sMCC), corresponding to harder granules. Moreover, in spite of using lubrication (magnesium stearate) on the tooling surfaces, rather high ejection forces were observed, which may cause problems during commercial tabletting, requiring further amelioration. Although the compacted gMgSm specimens were more porous, however, they still exhibited acceptable cohesive strengths, comparable to sMCC. Hence, there may be scope for using granular clay as one component of a tabletting formulation.

Following principles established in previous work, SAXS revealed information concerning the intragranular structure of the gMgSm and its response to compaction. The results showed that little compression of the intragranular morphology occurred below a relative density of 0·6, suggesting that granule rearrangements or fragmentation were the dominant mechanisms during this stage. By contrast, granule deformation became considerably more important at higher relative density, which also coincided with a significant increase in the cohesive strength of compacted specimens.

Spatially-resolved SAXS data was also used to investigate local variations in compaction behaviour within specimens of different shape. The results revealed the expected patterns of density variations within flat-faced cylindrical specimens. Significant variations in density, the magnitude of compressive strain and principal strain direction were also revealed in the vicinity of a debossed feature (a diametral notch) and within bi-convex specimens. The variations in compaction around the debossed notch, with a small region of high

density below and low density along the flanks, appeared to be responsible for extensive cracking, which could also cause problems in commercial tabletting.

INTRODUCTION:

The work presented here demonstrates the use of small-angle X-ray scattering (SAXS) to investigate the compaction of a granular clay powder. SAXS is typically measured at scattering angles below 5° and originates from electron density variations within materials due to structure on the scale of roughly 1 to 100 nm [Feigin and Svergun 1987, Roe 2000]. Hence, this method has been used extensively to investigate the morphologies of materials, including their responses to mechanical deformation. Nevertheless, the considerable capabilities of SAXS to investigate powder compaction behaviour were only revealed within the last few years [Laity and Cameron 2008, 2009]. It was observed that two-dimensional (2D-SAXS) patterns from various uncompacted polymeric powders were circularly symmetrical, as expected for randomly oriented granular materials. After compaction, however, the patterns became elongated in the compression direction, to an extent that increased with the applied pressure and the density achieved. This was ascribed to the Fourier transform from morphology to scattering [Feigin and Svergun 1987, Roe 2000], which gives a reciprocal relationship between length scales in real and scattering space. Hence, the changes in SAXS patterns were attributed to compressive strain of the intragranular morphologies, in response to the stress transmitted through intergranular contacts [Laity and Cameron 2010a]. Hence, by analysing SAXS patterns measured at different points across diametral sections from compacted specimens, it was possible to investigate variations in compaction behaviour associated with wall friction, specimen size and the shapes of the punches used [Laity and Cameron 2009, Laity et al. 2010a, Han et al. 2011, Laity 2014].

That work was largely inspired by the importance of powder compaction for pharmaceutical tabletting, which is the most popular and widely used formulation route for the majority of drugs [Aulton 2007]. Consequently, the behaviour of pharmaceutical excipients such as spheronised microcrystalline cellulose (sMCC), pre-gelatinised starch (PGS) and hydroxypropyl-methyl-cellulose (HPMC) was of major interest. Nevertheless,

compaction by the application of mechanical force or hydrostatic pressure also represents an important and widely used processing method for many granular materials across various industrial sectors, including metals [Liddiard 1984, German 2005, Kim et al. 2013] and ceramics [Rahman 2003, Pizette et al. 2013]. It would be interesting, therefore, to explore whether the SAXS method could also prove useful in studying the compaction behaviour of other materials.

The work reported here investigated the compaction behaviour of a commercial granulated magnesium smectite (gMgSm). Clays are important and widely-used industrial materials [Murray 2000, Bergaya et al. 2006], with potential applications as pharmaceutical excipients, [Aguzzi et al. 2007]. Hence, the present work was performed as part of a larger investigation into the feasibility of using granulated clay within tablet formulations [Asare-Addo et al. 2014]. Nevertheless, the compaction behaviour of clays is also important in many other situations; examples include the manufacture of ceramics [Rahman 2003, Pizette et al. 2013]; in building materials [Morel et al. 2007, Villamizar et al. 2012, Beckett et al. 2013]; in geology, where compacted clay layers can trap hydrocarbon deposits [Vanorio et al. 2003, Mondol et al.2007]; in soil mechanics, where compaction can affect the porosity of agricultural soil [Berisso et al. 2012, Romero 2013] and the behaviour of foundations [Kuklic 2011, Prakash et al. 2013]; as barrier materials for the storage of nuclear waste, where compacted clay gives low permeability [Tien et al. 2004, Ito 2006, Villar and Lloret 2008, Baille et al 2010, Ye et al. 2012, Villar et al. 2012].

It should be emphasised that SAXS measurements are generally performed at smaller angles than typical X-ray diffraction (XRD) measurements from crystalline materials. From the reciprocal relationship between scattering angle and length, this means that SAXS generally informs on structural features larger than typical crystalline spacings. Hence, the present work used measurements below 3° to investigate the larger scale structures within gMgSm granules and their responses to compaction. A distinction can be drawn between this and the study reported previously by Villar et al. [2012], which used measurements around 5° to investigate changes in the basal spacing of bentonites following compression at different water contents.

Although powder compaction may appear conceptually simple, a complete explanation of the underlying mechanics must address the frictional effects between granules and against the compaction tooling, the stochastic nature of intergranular contacts and the responses of granules to applied contact forces. Even in the simplest example of a flat-faced cylindrical specimen produced by single-ended compaction (i.e. the volume reduction occurs through displacement of one driven punch, while the other punch is static), local density variations occur due to friction against the tooling and the consequent granular flow pattern. The largest variations occur along the sides in contact with the die wall, with the highest density in a rim adjacent to the driven punch and the lowest density in a rim adjacent to the static punch. Smaller variations occur within the compact, with a high density zone in the centre of the compact just above the static punch and a low density zone below the centre of the driven punch.

This phenomenon was first explained by Train [1956], based on the movement of coloured layers within compacted magnesium carbonate powder beds. Similar results have also been obtained in many subsequent studies, using diverse materials and methods. These include further applications of the coloured layer method [Briscoe and Rough 1998], hardness measurements [Kandeil et al. 1997], autoradiography of radioactive materials [Macleod and Marshall 1977], magnetic resonance imaging (MRI) after perfusing with a non-swelling liquid [Nebgen et al. 1995] and X-ray microtomography (XμT) [Busignies et al. 2006].

The density variations obtained depend on the characteristics of the powder used – in particular, the friction coefficient and whether the granules respond by brittle fracture or plastic deformation. Consequently, powder formulations for compaction often involve mixtures of materials, including lubricants, binding agents and porogens. The situation is even more complex in pharmaceutical tabletting, which may also involve diluants and drugs with difficult compaction behaviour [Aulton 2007, Sinka et al. 2009].

The patterns of density variations depend on the shapes of the dies used and the profiles of the punch surfaces. Significant differences can be observed between flat-faced and convex punches, while dramatic effects can be produced by embossed features [Sinka et al. 2004, Djemai and Sinka 2006, Wu et al. 2008, McDonald et al. 2009, Laity et al. 2010a, Han et al. 2011, Laity 2014]. The density variations can also be affected by the

compaction method; friction against the die walls during single-ended compaction causes distinct asymmetry between the static and driven faces, while double-ended compaction (i.e. the displacement is applied equally through two opposing punches) produces more symmetric patterns.

Density variations within compacted artefacts are important for several reasons. Generally, low density is linked to poor strength and an increased likelihood of mechanical failure. Large local variations in compaction behaviour can also lead to crack formation [McDonald et al. 2009]. Clearly, these effects are undesirable where significant load-bearing is a crucial element in the desired function (e.g. in some engineering parts or the foundations of buildings), but may also affect how easily products become damaged in subsequent handling (e.g. chipping of pharmaceutical tablets during packaging and transportation). Moreover, where compaction occurs as part of a sintering process, low density equates to high porosity, which may be linked to dimensional instability during subsequent processing. Conversely, however, maintaining adequate porosity may also be an important property (e.g. for aeration and drainage of agricultural soil; permeability of catalytic supports, filters and 'self-lubricating' bearings). In the case of pharmaceutical tablets, low porosity may impede disintegration and delay the drug delivery [Aulton 2007, Laity and Cameron 2010b].

In view of the wide diversity of situations where powder compaction is important, this presents enormous scope for scientific investigation and has resulted in numerous publications, although a comprehensive review is well outside the scope of this paper.

The present work examined the compaction behaviour of gMgSm at several levels. Firstly, XRD was used to reveal the crystal structure of gMgSm and the granule structure was investigated by SEM. Bulk compaction behaviour was examined through measurements of average punch pressure against relative density and the structures of the compacted specimens were examined using XμT. The main part of the work used SAXS to relate macroscopic compaction behaviour to morphological responses of granules at the nanometre scale. This was based on methods developed previously using polymeric excipients, but provided a 'proof of principle' for studies on gMgSm, which has a very different chemical composition. Having established

relationships between compaction behaviour and changes in SAXS patterns, local variations were explored by spatially resolved SAXS mapping measurements.

EXPERIMENTAL:

The work reported here was performed using a commercial granulated clay (Veegum G®, R.T Vanderbilt Co. Inc.), extracted from Arizona, California and Nevada, USA, consisting of magnesium smectite (gMgSm). This material was part of a sample supplied by Lake Chemicals and Minerals Ltd. (Redditch, UK). The true density (ρ) of the gMgSm. determined using helium pycnometry (Ultrapyconometer, Quantachrome Instruments, UK) was 2499 ± 23 kg m^{-3}.

X-ray diffraction:

The gMgSm was characterised by X-ray diffraction (XRD) using a D2 Phaser diffractometer (Bruker AXS GmbH, Karlsruhe, Germany), with a sealed microfocus generator operated at 30 kV and 10 mA, producing $Cu_{K\alpha}$ (λ_X = 0·1542 nm) radiation and a Lynxeye 'silicon strip' multi-angle detector. The specimen was scanned in Bragg-Brantano geometry, over a scattering (Bragg, 2θ) angle range from 5 to 100°, in 0.02° steps at 1·5° min^{-1}.

Scanning electron microscopy:

The gMgSm granule structure was examined using a Quanta 200 3D dual beam scanning electron microscope (SEM, FEI, Hillsboro, OR, USA). A small amount of powder was transferred onto an electron microscope stub using compressed air to 'spray' the granules onto an adhesive carbon pad; this ensured an even dispersion across the surface. To reduce the charging effects normally experienced when investigating such granules in conventional high vacuum mode, the microscope was operated in low-vacuum mode, at a pressure of 70 Pa. Secondary electrons were collected using the 'large area detector', at a working distance of ca 4 mm from the pole-piece. The electron beam energy was 20 keV and the electron beam current used was 0·6 nA.

Compaction experiments:

Compaction experiments were performed using polished stainless steel dies of circular cross-section (internal radius R = 5·00 mm) and closely-fitting flat-faced punches (Specac, Orpington, UK). Before each experiment, the tooling was lubricated by painting the surfaces with a 1% dispersion of magnesium stearate in acetone. A pre-weighed amount of powder (ca. 0·80 g) was poured into the die and loosely packed by gently tapping against the bench. Compaction was performed to a pre-set peak force (F_{max}) of up to 16 kN, using a computer-controlled mechanical testing machine (M500-50CT, Testometric Co. Ltd. Rochdale, UK), fitted with compression platens. The filling depth (h_0) of the powder bed was determined from the starting cross-head position. The compaction rate was determined by the movement of the cross-head, which was set at 3 mm min^{-1} during the compression stage. The force (F) was transmitted through a push-rod between the load cell and the upper punch, while the lower punch remained stationary. The upper punch displacement was measured using a linear variable differential transformer (LVDT) position gauge attached to the platens. As soon as the required peak force had been achieved, the upper punch was allowed to retract at 1 mm min^{-1}.

Force and displacement (F(t) and x(t), as functions of time) were recorded automatically, at 0·2 s intervals during the experiment. The compliance (i.e. apparent displacement under load) of the apparatus was determined as a function of applied force, by performing the compaction on an empty die and fitting a suitable curve to the results; this was subsequently used to correct the recorded displacement. In the case of compaction experiments to prepare standard flat-faced specimens, the average pressure across the upper punch was calculated from:

$$P(t) = \frac{F(t)}{\pi R^2} \tag{1}$$

and the average relative density of the compacted bed was calculated using:

$$\rho_{rel}(t) = \frac{m}{\rho \pi R^2 [h_0 - x(t)]} \tag{2}$$

where m is the mass of the specimen (measured after ejection).

Once the applied force had returned to zero, the specimen was promptly ejected from the die in the same direction as the initial compaction, using the mechanical testing machine at 5 mm min^{-1}. The height and diameter of the ejected specimen were measured promptly, using callipers with a vernier scale (to ± 0·02 mm) and the mass was determined using a 4-figure top-pan balance (to ± 0·0003 g).

Different punches were also used in order to investigate the effects of contact surface shape. Bi-convex specimens were prepared using concave punches (13·5 mm radius of curvature), which were made in the machining workshop, at the University of Cambridge, Department of Materials Science and Metallurgy. Specimens with a debossed furrow were prepared using an upper punch with a rounded ridge (1 mm wide × 0·75 mm high) across its diameter, which was made by KWI Grinding Ltd. (Coventry, UK).

In order to calibrate the SAXS measurements over a suitable range of compaction pressures, smaller flat-faced cylindrical specimens (R = 2·5 mm) were also produced in a similar way, by compacting powder (ca. 0·1 g) using F_{max} from 2 to 12 kN, (corresponding to P_{max} from 102 to 611 MPa). Given the size and mass of the calibration specimens, an experimental uncertainty of ± 0.011 was estimated for the relative densities of these calibration specimens.

Cohesive strength measurements

The cohesive strengths (σ_C) of flat-faced specimens prepared using the larger (R = 5·0 mm) die were obtained from the peak diametral crushing force (F_C):

$$\sigma_C = \frac{F_C}{\pi R_S h_S} \qquad (3)$$

where R_S and h_S are the radius and thickness of the specimen respectively [Aulton 2007]. It should be noted that, as a result of elastic recovery after ejection, the specimen radius was generally slightly larger than the die radius.

XμT examination of compacted specimens:

Compacted specimens were examined by XμT, (Nikon XT H 225, Nikon Corp. Tokyo, Japan), using a tungsten target, with 75 kV accelerating voltage and 250 μA gun current. A copper filter (thickness 0·125 mm) was positioned just in front of the 1024×1024 pixel detector. The specimen was mounted onto the sample stage using a small patch of double-sided adhesive tape. A set of 720 projections was collected, with 2 frames per projection and 354 ms exposure per frame, giving a total time of roughly 22 min for the complete XμT acquisition. The set of projection images was reconstructed using CT-Pro, then examined using VG Studio 2.1 software.

SAXS measurements

SAXS measurements were performed using a Nanostar system (Bruker AXS GmbH, Karlsruhe, Germany). X-rays (Cu_{Ka} λ_X = 0·1542 nm) were produced using an air-cooled microfocus generator (Incoatec GmbH, Geesthacht, Germany), which was operated at 50 kV and 0·6 mA. The X-rays were collimated into a parallel beam (ca. 0·9 mm diameter spot-size on the specimen), using a pair of Göbel mirrors and a three-pinhole system. A circular beam-stop was suspended just before the centre of the detector, to block the high intensity of the undeviated X-ray beam. The sample-to-detector distance was approximately 1·07 m and the entire optical path was evacuated, to minimise the scattering background.

Two-dimensional scattering (2D-SAXS) patterns were collected using a Vantec-2000 (2048 × 2048 pixel) area detector. As is common practice for SAXS, no intensity calibration was performed and the intensity data shown here is presented in 'arbitrary units'. Calibration of the scattering angle (2θ) was obtained using the peaks from a silver behenate reference standard. The scattering range was then calculated in terms of the modulus of the scattering vector:

$$q = |\mathbf{q}| = \frac{4\pi}{\lambda_X} \sin\theta \qquad (4)$$

Diametral sections (thickness 1.0 mm) were prepared by shaving specimens with a scalpel and rubbing against abrasive cloth (P180 grade). Each section was mounted on the computer-controlled sample stage, using double-sided adhesive tape along its bottom edge. 2D-SAXS patterns were collected in transmission geometry, using collection times of 2000 s. It may be noted that thinner sections and longer collection times were used in the present work, compared with previous studies on MCC and other organic excipients, to compensate for the stronger X-ray absorbance of the gMgSm.

The background scattering pattern for the empty SAXS apparatus was also collected under similar conditions. After correcting for sample transmission, using a glassy carbon filter to scatter the transmitted light, the background corresponded to considerably less than 1% of the scattering from a gMgSm specimen. Hence, further background correction was generally considered unnecessary.

For mapping experiments, the co-ordinates for the desired SAXS measurements were programmed at intervals of 0·5 mm in both the horizontal and vertical directions. As in previous work, data was not collected from a margin of about 0·5 mm around the edges of the diametral sections, where SAXS measurements were 'contaminated' by X-ray reflection spikes or part of the scattered beam emerging more quickly through the sides of the specimen, producing differences in absorbance.

Analysis of SAXS data:

Initial processing of the two-dimensional patterns was performed using the GADDS software provided (Bruker AXS GmbH, Karlsruhe, Germany). One-dimensional radial scans were extracted from the 2D-SAXS patterns by integrating over azimuthal arcs of ϕ = 20° (i.e. ± 10° of the desired direction), from 2θ = 0 to 3°, using normalisation by arc length. Azimuthal scans (i.e. along a circular path, around the centre of the 2D-SAXS pattern) were extracted by integrating over the range 2θ = 0·2 to 0·6° (corresponding to q = 0·142 to 0·427 nm^{-1}), from ϕ = 0 to 360°. In either case, the results were exported as text files and all subsequent analyses were performed using Excel (Microsoft Corp. Redmond, WA, USA).

Further analysis of the SAXS data to extract information on compaction behaviour followed the basic methods reported previously (Laity and Cameron 2008, 2009, 2010a), as summarised below.

RESULTS:

In order to examine the crystal structure, the XRD pattern obtained for the gMgSm is shown in Figure 1. Comparison with published data for Source Clay specimens (Chipera and Bish, 2001) indicated similarity to clays from Gonzales County, Texas (STx-1) and Crook County, Wyoming (SWy-2), consisting of smectite (ca. 67 to 95%) together with quartz, feldspar and minor amounts of other materials.

The majority of reflections in the measured XRD pattern were generally quite broad, consistent with small or distorted crystallites. For the relatively intense reflections at $2\theta = 19{\cdot}8°$ and $21{\cdot}9°$, the breadths (i.e. full width at half peak height, β) were around $0{\cdot}5°$; interpretation of this using the Scherrer equation (Hammond 1997):

$$w = \frac{\lambda_X}{\beta \cos\theta} \tag{5}$$

suggested a crystallite size of $w \approx 18$ nm. This estimate should be regarded as a minimum size, however, as crystal distortion (i.e. variations in layer spacings) due to other factors (e.g. mechanical stress, changes in composition or defects) may also cause peak broadening.

The basal reflection around $2\theta \approx 8{\cdot}3°$ appeared particularly broad ($\beta = 1{\cdot}8°$), indicating very small size ($w \approx 5{\cdot}5$ nm) or poor registration between these crystallographic planes. This may have been due to variable amounts of water or mixtures of exchangeable ions in the interlayer spaces causing variations in their separation. The periodicity (d) can be obtained from the scattering angle using the well-known Bragg equation [Hammond 1997]:

$$d = \frac{n\lambda_X}{2\sin\theta} \tag{6}$$

where n is an integer corresponding to the order of the reflection (i.e. n = 1 for 1st order reflections). This gave d ≈ 10·7 Å, which appears consistent with the expected basal spacing for a smectite without hydration (Bergaya et al. 2006, Moyano et al. 2012, Villar et al. 2012).

Further investigation into crystallographic changes of gMgSm in response to powder compaction, including some of the effects of hydration considered previously by Villar et al. [2012], could be a very fruitful area for further work, although it was outside the scope of the present work. It should be noted that SAXS reported on structural elements larger than typical crystal plane spacings; in the context of gMgSm, this could include crystallites (i.e. particles or assemblies of crystallographic layers) and assemblies of particles (i.e. aggregates), together with inter-particle and inter-aggregate pores.

SEM images of typical gMgSm granules are shown in Figure 2. Examination at lower magnification (Figs. 2a and b) showed that the granules were polydispersed, with diameters between 40 and 150 µm. Although the outlines were irregular, the granules generally appeared to be roughly isometric, with aspect ratios (i.e. length of major to minor axis) of less than 1·5. These observations suggest that the gMgSm granules were unlikely to adopt a preferred orientation due to their original shape, during die-filling or subsequent compaction.

The granules also appeared to have aggregated internal structures, composed of smaller particles. Examination at higher magnification (Figs. 2c and d) suggested the presence of porosity and structural elements with dimensions significantly below 1 µm. Granulated powders such as this often show improved compaction behaviour, compared with powders composed of larger solid particles. Moreover, the aggregated internal structure of the granules was likely to be the origin of the observed SAXS, as found previously with PGS and sMCC [Laity et al. 2010b].

Bulk compaction behaviour:

The bulk compaction behaviour of gMgSm is demonstrated in Figure 3a, as plots of the average punch pressure vs. relative density during loading and unloading. Very good reproducibility was obtained for experiments performed in duplicate, with the plots overlaying closely. Moreover, no significant differences in

compaction behaviour were observable between experiments performed in the smaller and larger dies; this is demonstrated by comparing the compaction curves to P_{max} = 204 MPa (R = 5·0 mm) and the corresponding section of the curve to P_{max} = 611 MPa (R = 2·5 mm). The only difference was attributable to the slightly higher uncertainty in relative densities for the smaller specimens (± 0·011 for R = 2·5 mm, c.f. ± 0·004 for R = 5·0 mm).

Prior to compaction, the loosely filled powder achieved a relative density of around 0·32. Subsequently, the punch pressure increased progressively more quickly as the relative density was increased, attaining values of 0·88 (± 0·004) and 0·95 (± 0·011) at peak pressures of 204 and 617 MPa respectively. The shape of the loading curve for gMgSm was similar to those reported elsewhere for HPMC, PGS and sMCC under similar conditions [Laity and Cameron 2008, 2009], except that those organic excipients compacted more easily, giving higher densities at comparable punch pressures (e.g. 0·93 to 0·96 at 200 MPa).

The compaction behaviour during the loading stage was dominated by plastic (i.e. non-reversible) effects, which may be ascribed to granular movement, fragmentation and deformation. After reaching the required value of P_{max}, however, gMgSm exhibited significant elastic recovery during unloading. The data in Figure 3a show a reduction in relative density of 7% (i.e. from 0·88 to 0·81) for the specimens compacted at 204 MPa or 10% (i.e. from 0·95 to 0·85) for the specimens compacted at 611 MPa. This was considerably larger than the recovery observed previously for common tabletting excipients (typically 3%, for PGS and sMCC samples compacted to 250 MPa). The larger recovery shown by gMgSm was surprising for a material that was expected to compact in a predominantly brittle manner. On the contrary, this may indicate significant elastic behaviour for gMgSm, involving (reversible) deformation of the various structural elements making up the granules. In this respect, changes in the basal plane spacing, either through direct compression or bending of the crystals may have been an important factor. This could be investigated further by XRD, although it was outside the scope of the present work.

In spite of using lubrication, rather high ejection forces were observed with gMgSm (often exceeding 3 kN for a 10 mm diameter specimen). This suggested that considerable radial force remained between the compacted

specimen and the die walls. Moreover, it was generally observed that the ejected gMgSm specimens consistently had diameters around 1% larger than the (R = 2·5 or 5·0 mm) die used. These observations also suggested significant elastic behaviour of the gMgSm during compaction.

In order to investigate this further, the constrained modulus (M) of the compacted gMgSm within the die was evaluated from the initial (i.e. approximately linear) part of the elastic recovery observed in the compaction experiments. The true (i.e. logarithmic or Hencky) compressive strain of the powder bed can be calculated from the incremental change in relative density, which is related to the depth of the bed:

$$\mathrm{d}\varepsilon_{\mathrm{macro}} = -\frac{\mathrm{dx}}{\mathrm{x}} \tag{7a}$$

After integration and some further manipulation, this gives:

$$\varepsilon_{\mathrm{macro}} = \ln\left(\frac{\rho_2}{\rho_1}\right) \tag{7b}$$

where ρ_1 and ρ_2 refer to the initial and final states and a positive value indicates compaction.

The measured changes in average punch pressure and strain during recovery gave M = 4·0 ± 0·4 GPa at ρ_{rel} = 0·87 (using P_{max} = 204 MPa), rising to 12·7 ± 0·6 GPa at ρ_{rel} = 0·93 (using P_{max} = 611 MPa). The relationships between constrained modulus, Young's modulus (E) and bulk modulus (K) are described by:

$$\mathrm{M} = \frac{\mathrm{E}(1-\nu)}{(1-2\nu)(1+\nu)} \tag{8a}$$

$$\mathrm{K} = \frac{\mathrm{E}}{3(1-2\nu)} \tag{8b}$$

$$\mathrm{K} = \frac{\mathrm{M}(1+\nu)}{3(1-\nu)} \tag{8c}$$

where ν is Poisson's ratio. Hence, the results obtained here for gMgSm agreed reasonably well with previously published results for compacted clays [Vanorio et al. 2003, Mondol et al.2007, Moyano et al. 2012] and were somewhat larger than expected for sMCC, based on data previously reported by Han et al.

[2011]. The smaller modulus of sMCC suggests that it should exhibit greater strain during loading and unloading than gMgSm, which is counter to the observations. Consequently, it appeared that the differences in elastic recovery between these materials could not be ascribed simply to the moduli.

In view of the problems that can arise in tabletting due to elastic recovery and crack formation or excessive wear of the tooling due to high frictional forces, these aspects of gMgSm compaction behaviour merit further investigation. For example, amelioration may be possible by using mixtures of gMgSm with softer excipients.

The relationship between the relative densities of ejected gMgSm specimens and the peak punch pressures used is shown in Figure 3b. The vertical error bars represent the uncertainties in the relative density values due to the expected errors in measuring the sizes and masses of for the larger (± 0·004) and the smaller specimens (± 0·011) that were used in order to access the higher compaction pressures.

Both sets of specimens followed the same trend. The results showed a relatively rapid increase in ρ_{rel} up to around 0·82 at 300 MPa, followed by progressively smaller increases at higher peak punch pressures. Similarly shaped curves were also reported previously for HPMC, PGS and sMCC [Laity and Cameron 2008, 2009] although, as previously noted, these organic excipients achieved significantly higher relative densities than the gMgSm at comparable pressures. Moreover, it appeared that gMgSm resisted complete compaction; even the highest peak pressure used (P_{max} = 617 MPa) resulted in ejected specimens with around 15% pore volume fraction.

It may be noted that the calculated values of relative densities also depended on the value used for the true density of gMgSm. A value of 2499 ± 10 $kg.m^{-3}$ was obtained by helium pycnometry, which is consistent with previously published values for montmorillonite [Lide 2002, Vanorio et al. 2003]. Nevertheless, the accuracy of true density measurements using gas pycnometry has been questioned [Sun 2004], particularly for hydrated materials. This could produce systematic errors in the absolute relative density values quoted, although comparisons between different compaction conditions would still be valid.

Cohesive strength:

The relationship between relative density and cohesive strength (i.e. tablet hardness), measured for compacted gMgSm in flat-faced cylindrical specimens, is shown in Figure 4. The horizontal error bars (± 0·004) reflect the relatively small errors expected in determining the relative densities of the (R = 5·0 mm) specimens used for these measurements, while the vertical error bars (± 100 kPa) reflect the typical variations in breaking strength obtained for three nominally identical specimens.

Below a relative density of 0·58 (corresponding to P_{max} = 38 MPa), only relatively weak specimens were produced (σ_c < 235 kPa), which crumbled easily. The cohesive strengths increased rapidly at higher relative densities, however, giving values around σ_c = 2·3 MPa at ρ_{rel} = 0·79 (corresponding to P_{max} = 191 MPa). To put these results in the context of tabletting, comparisons may be made with an excipient such as sMCC, which is commonly used as a binder at 20 to 90% in tablets. When compared on the basis of relative density, the gMgSm specimens were significantly stronger than sMCC specimens, which achieved values of $\sigma_c \approx 1{\cdot}6$ MPa at ρ_{rel} = 0·79. This suggests that tablet formulations based on gMgSm may be more robust and less prone to damage during subsequent handling. As the sMCC was considerably easier to compact than gMgSm, however, this strength was achieved at significantly lower P_{max} = 125 MPa (i.e. only $^2/_3$ the peak compaction pressure required for gMgSm). It should be noted that these results represented the average values for flat-faced cylindrical specimens. Hence, local density variations associated with debossed features or curved punches may impact on the cohesive strengths and susceptibility to damage of shaped tablets.

The balance between compaction pressure, relative density and cohesive strength also requires further investigation, particularly as gMgSm is likely to be used as a component in mixtures of excipients, in order to ameliorate the adverse effects of high friction and elastic recovery revealed by the compaction experiments. These characteristics may also be affected by the presence of drugs in pharmaceutical formulations and their physical interactions with the clay. For example: Pongjanyakul and Rojtanatanya [2012] observed differences in tablet hardness and drug release profiles for propranolol hydrochloride as physical mixtures or intercalated complexes in magnesium aluminium silicate. Physical mixtures exhibited anomalous transport behaviour,

while zero-order release rates were observed for the complexes, suggesting that these show potential as drug reservoirs in polymeric matrix tablets. Clearly, investigating these effects amongst the vast number of potential formulations presents a major research opportunity, but is beyond the scope of the present work.

XμT examination of gMgSm compacts:

Reconstructed diametral cross-sectional images obtained by XμT examination of compacted gMgSm specimens (using P_{max} = 204 MPa) are presented in Figure 5. This technique was based on the differential absorbance of X-rays between materials of differing electron density [Stock 1999, Baruchel et al. 2000]. In the case of compacted granular materials, absorbance can depend on local variations in mass density; hence, it was expected that more highly compacted materials should absorb more strongly and appear darker in the reconstructed images. In practice, however, the image quality was considerably degraded due to beam hardening and only the most extreme instances of density variations were evident by XμT.

A diametral section through a flat-faced cylindrical specimen is shown in Figure 5a. The image showed short-range variations in X-ray absorbance, which may be associated with the granular packing. It was not possible to find any evidence of the expected longer-range density variations, however, probably because these were relatively small and produced insufficient X-ray contrast to observe by XμT.

XμT did reveal the more extreme density variations within the notched and bi-convex specimens (Figures 5b, c and d). Closer examination also revealed extensive cracking radiating from the flanks of the notch and extending over the entire diameter of the specimen (Figures 5d and e). This may also have been caused by significant elastic recovery on unloading, possibly in conjunction with local density variations around debossed features, as the average cohesive strengths of the compacted gMgSm specimens appeared adequate.

SAXS analysis of compaction behaviour:

Typical 2D-SAXS data for gMgSm are shown in Figure 6. The pattern for the uncompacted specimen (Figure 6a) exhibited circular symmetry, indicating no preferred orientation of the nanometre-scale morphology, as expected for a powder with randomly oriented granules. By contrast, the 2D-SAXS patterns

for compacted specimens (Figure 6b and c) appeared significantly elongated in the vertical (i.e. compaction) direction, consistent with the morphology becoming compressed in that direction.

Although precise normalisations were not performed, all the specimens were of similar thickness and similar acquisition conditions (i.e. spot size, illumination intensity, acquisition times, detector response) were used. Hence, semi-quantitative comparisons between SAXS patterns for the different specimens were possible. In addition to the patterns becoming elongated, the overall intensity decreased with the compaction pressure, due to the X-ray absorbance increasing with the bulk density. This change in absorbance affected the scattered X-ray intensity equally in all directions, however; consequently, it was not responsible for the changes in shape of the SAXS patterns.

A radial intensity plot for the uncompacted gMgSm powder is shown in Figure 6d. This followed a smooth curve of decreasing intensity, from the edge of the beam-stop shadow (at $2\theta = 0{\cdot}14°$, corresponding to $q \approx 0{\cdot}1$ nm^{-1}) to the outer limit of the detector (at $2\theta = 3{\cdot}2°$, $q \approx 2{\cdot}275$ nm^{-1}). No scattering features (e.g. peaks) associated with specific structures were observable.

A comparison with the background scattering intensity (measured for the empty SAXS apparatus) is also shown in Figure 6d. The Vantec-2000 detector gave a relatively 'clean' background, with minimal electronic noise. Moreover, as a result of the relatively strong scattering and absorbance of the gMgSm, the background intensity (after scaling to correct for sample absorbance) was between 2 and 5 orders of magnitude lower than that measured for the samples. Subtraction of this suitably scaled background from the sample scattering produced only negligible changes; hence, background subtraction was generally considered to be unnecessary.

Examples of scattering data for gMgSm are also shown in Figure 7, in the form of double-logarithmic plots of intensity against the modulus of the scattering vector. Again, the absence of any features (peaks or significant changes in slope) in the SAXS intensity plots should be emphasised. In each case, the data followed essentially straight lines, indicating power-law scattering behaviour

$$I(q) = I_0 q^{-\alpha} \tag{9}$$

where I_0 is a constant that depends on various factors (incident X-ray intensity, strength of scattering, irradiated sample volume, collection time etc.) and α is the power-law constant, which depends on the morphology of the specimen. A slope of -3·2 was obtained for uncompacted gMgSm powder (Figure 7a), while slightly lower slopes between -2·89 to -3·01 were found for the compacted specimens (Figure 7b). Moreover, while the compacted specimens exhibited stronger scattering in the compression direction than transverse direction, the same power-law behaviour was obtained in each direction (i.e. the compression direction and transverse direction plots in Figure 7b have the same slopes).

Power-law scattering dependence may be attributable to a fractal-like morphology with its dimension related to the power-law constant, as described by Schmidt [1991], Oh and Sorensen [1999], Roe [2000] and Sorensen [2001]. For a strictly two-phase fractal system, the scattering is expected to obey one of the following equations:

$$I(q) = I_0.q^{-D_M} \qquad \text{with:} \quad 0 < D_M \leq 3{\cdot}0 \tag{10a}$$

or $$I(q) = I_0.q^{-(6-D_S)} \qquad \text{with:} \quad 2{\cdot}0 \leq D_S < 3{\cdot}0 \tag{10b}$$

where D is the fractal dimension and the subscripts refers to a mass- or surface-fractal. For scattering with a power-law constant of around 3, however, neither case would appear to make physical sense; a mass-fractal with $D_M = 3{\cdot}0$ or surface-fractal with $D_S = 3{\cdot}0$ would both be completely space-filling and should give no scattering in the SAXS range.

In reality, however, the precise nature of a fractal-like structure may not be entirely clear based on the value of the power-law constant alone. For a hybrid system of scattering elements with overall domain (i.e. aggregate or cluster) size (Z_D) and distance between individual scattering centres ($2z_s$), the power-law constant can depend on both surface and volume fractal dimensions [Oh and Sorensen 1999, Sorensen 2001]:

$$\alpha = 2D_M - D_S \tag{11a}$$

$$\text{for:} \qquad Z_D^{-1} < q < z_s^{-1} \tag{11b}$$

This appears to provide ample scope for power-law behaviour with $\alpha \approx 3{\cdot}0$, in the form of:

$$D_M = 1.5 + \frac{D_S}{2} \qquad (11c)$$

As noted previously [Oh and Sorensen 1999, Sorensen 2001], simple two-phase fractal aggregate systems are all surface, with $D_S = D_M$, which cannot give $\alpha = 3$. Hence, the nanometre-scale morphology of the gMgSm granules must be somewhat more complex, perhaps incorporating fractal surfaces with irregular internal density fluctuations or multiple compositional phases, with polydispersed length scales. For example, Oh and Sorensen [1999] calculated the scattering from a model system consisting of point scatterers randomly displaced from a square lattice within a circular domain, which showed q^{-3} dependence over a considerable scattering range.

Some broad deductions could be made concerning the sizes of morphological features, based on Equation 11b. As the double-logarithmic SAXS plots followed essentially the same gradient over the entire q-range used, this was consistent with the minimum spacing between scattering elements of $2z_s < 0{\cdot}88$ nm and overall domain size of $Z_D > 10$ nm. It should be noted that this minimum spacing was similar to the basal layer periodicity deduced from XRD; hence, it seems likely that single aluminate-silicate layers may have constituted the scattering centres responsible for the SAXS. At the other extreme, the overall domain size may have approached the sub-microscopic structures observed by SEM.

It was not possible, however, to make any firm conclusions regarding the compositions of the morphological features responsible for the scattering, based on SAXS alone. In general, SAXS arises due to patterns of electron density variations over nanometre-scale lengths; the associated differences in chemical compositions are of secondary importance, although the chemistry may affect the magnitude of these variations and, hence, the strength of scattering [Feigin and Svergun 1987, Roe 2000]. For the gMgSm material used here, the fundamental nanometre-scale structural elements were expected to consist of layers or particles of inorganic clay mineral layers and interlayer porosity, whereas elementary crystals of cellulose or starch molecules and pores appeared to be the main components of the materials studied previously [Laity and Cameron 2010b].

Nevertheless, with respect to investigating the compaction behaviour, knowing the precise morphology was less important than the occurrence of power-law scattering behaviour, on which the analysis is based. A full discussion of this is given in a previous publication [Laity and Cameron 2008, 2009, 2010a] and only a summary is presented here.

It was suggested that the macroscopic compaction of the powder was accompanied by affine deformation of the structural elements constituting the intragranular morphology. This could be represented by initially spherical domains in the uncompacted granules becoming ellipsoidal, with corresponding decreases in the characteristic lengths of the structural elements responsible for the SAXS in the compression direction. Through the scaling property of the Fourier transform and the power-law scattering dependence, a relationship was obtained between the intensities in the compression and transverse directions [Eqn. 12 in Laity and Cameron 2010a]:

$$I_{comp}(q) = I_{trans}(q)\,b^{-\alpha} \tag{12}$$

where α is the power-law constant obtained from the double-logarithmic plots of SAXS data and b is a 'compression ratio' that describes the change in characteristic lengths (L) between the compression and transverse directions:

$$b = \frac{L_{comp}}{L_{trans}} \tag{13a}$$

$$= \left\{ \frac{I_{trans}(q)}{I_{comp}(q)} \right\}^{1/\alpha} \tag{13b}$$

Consistent with this, it was found that the data measured in one (i.e. the compaction or transverse) direction could be scaled using Equation 12 to fit the intensity measured in the 'other' direction. This is demonstrated in Figure 7b, with scattering data for a sample compacted to 255 MPa (achieved with α = 2·92 and b = 0·847).

Following the 'affine deformation' hypothesis of initially spherical morphological elements, it was also found that azimuthal intensity variations could be fitted using the model described by:

$$R(\phi) = \frac{I(q,\phi)}{I_{trans}(q)} \tag{14a}$$

$$= \frac{\left(b^2 \sin^2\phi + \cos^2\phi\right)^{\alpha/2}}{b^{\alpha}} \tag{14b}$$

This is demonstrated in Figure 8, using data for a sample compacted to 255 MPa. Moreover, good agreement was obtained between the values of b estimated using both methods (Equations 13 and 14) for a range of specimens of different ρ_{rel} (i.e. produced using different P_{max}).

These results for gMgSm were remarkably similar to those observed previously using HPMC, sMCC and PGS [Laity and Cameron 2008, 2009, 2010a]. At first sight, this may seem surprising as the chemical composition of gMgSm was clearly different from those polymeric excipients. It should be emphasised, however, that the SAXS originated predominantly from the nanometre-scale intragranular morphologies. Hence, at this level of morphology, it would appear that the gMgSm exhibited similarities to the structures observed previously in sMCC and PGS granules [Laity et al. 2010b], irrespective of their different chemical compositions. Moreover, it appeared that these intragranular morphologies responded similarly during compaction, suggesting that the analyses developed previously for the polymeric excipients might also be applicable to gMgSm.

Azimuthal intensity variations were quantified using the Hermans orientation parameter [Roe 2000]:

$$H = \frac{3\left\langle \cos^2\phi \right\rangle - 1}{2} \tag{15a}$$

where:
$$\left\langle \cos^2\phi \right\rangle = \frac{\int_0^{360} I(\phi).\cos^2\phi.|\sin\phi|.d\phi}{\int_0^{360} I(\phi).|\sin\phi|.d\phi} \tag{15b}$$

and ϕ is the azimuthal angle. The integrations were performed numerically, with angular intervals of $d\phi = 1°$.

The relationship between the Hermans parameter and the peak compaction pressure used is shown in Figure 9a, while the relationship to the relative density achieved is shown in Figure 9b. In each case, the vertical error bars represent the typical variation (± 0·004) in measuring H for nominally identical specimens, while the horizontal error bars in Figure 9b represent the uncertainty in relative densities (± 0·011) for the (R = 2·5 mm) specimens used to access the higher punch pressures. Measurements were only made for P_{max} between 100 and 600 MPa, corresponding to ρ_{rel} between 0·73 and 0·86. Below this range, the specimens were too weak and prone to fragmentation during sectioning. Above this range, there was considered to be an unacceptable risk of damage to the surface of the die, due to the large ejection forces experienced with gMgSm.

The azimuthal intensity variations increased with the extent of compaction, as represented by the peak upper punch pressure used (Figure 9a) or the relative density achieved (Figure 9b). This can be interpreted as a progressive compression of the nanometre scale morphology, in tandem with the macroscopic compaction. Both plots also showed curvature over the ranges explored; the slope of plot in Figure 9a decreased at higher pressure, while it increased at higher relative density in Figure 9b. This can be attributed to the increased resistance to further compaction, as the relative density increased, which was demonstrated in Figure 3. Moreover, while the relationship between relative density and peak pressure (Figure 3b) flattened out above 300 MPa, the plot of H vs. P_{max} appeared to continue rising above 600 MPa. Hence, it appeared that analysis of SAXS data provided a method for estimating the compressive stress in more highly compacted specimens.

Mathematical models of suitable shape were fitted to the data by a standard procedure of minimising the squares of the deviations; the resulting best fits are indicated by the continuous lines in Figures 9a and 9b. Hence, it was found that the relationships between H and ρ_{rel} or P_{max} could be described by the equations:

$$P_{max} = 20 + 500H + 6\exp\left(\frac{H}{0.021}\right) \quad (16a)$$

$$\rho_{rel} = 0\cdot412 + 8.87H - 43.98H^2 - 2.096H^3 \quad (16b)$$

These equations were subsequently used to extract results from mapping measurements. It should be noted, however, that while the shapes of these curves reveal aspects of the compaction behaviour of gMgSm powder, the equations are entirely empirical and offer no explanation of the underlying compaction mechanisms. Different forms giving similar shapes would be equally valid.

The true compressive strain corresponding to the macroscopic compaction of the powder was calculated using Equation 7. In an analogous way, a compressive strain can be calculated based on the compression ratio obtained from SAXS data using Equations 13 or 14:

$$\varepsilon_{\text{nano}} = -\ln(\text{b}) \tag{17}$$

As the SAXS originated from electron density variations on the nanometre scale, within the gMgSm granules, this describes the compressive response of those features (nanostrain) during compaction. Hence, a distinction can be drawn between this nanostrain and the macroscopic compression behaviour of the powder bed, which may also involve mechanisms such as granule fragmentation and changes in packing that do not affect the intragranular morphology or the shapes of 2D-SAXS patterns.

Changes in nanostrain during compaction are shown in Figure 10. The nanostrain values were obtained from SAXS data measured close to the centres of 2·5 mm radius specimens and are expected to represent median values. As expected, the nanostrain increased with the degree of compaction, which is represented by the relative density in Figure 10a or the corresponding macrostrain in Figure 10b. In both cases, the data appeared to follow well-defined trends (shown by the dashed lines in Figure 10), with most deviations being within the experimental uncertainty.

Considerable disparity was observed between nanostrain and macrostrain, however, as demonstrated in Figure 10b. The slope of the graph below $\varepsilon_{\text{macro}} = 0{\cdot}95$ appeared to be around 0·5, which suggested that other compaction mechanisms (granule rearrangement and fragmentation) contributed to the increase in bulk density or macrostrain, but did not affect the intragranular morphology or nanostrain. Moreover, extrapolation to lower values suggested that nanostrain only occurred for $\rho_1 > 0{\cdot}58$, corresponding to $\varepsilon_{\text{macro}} > 0{\cdot}60$; presumably, the

other mechanisms dominated at lower degrees of compaction. It may also be relevant that this degree of compaction roughly coincided with the point at which cohesive stress started to increase rapidly (see Figure 4), suggesting that granule deformation may be necessary to produce stronger specimens.

The graph appeared to become significantly steeper for $\varepsilon_{macro} > 0{\cdot}95$, however, indicating that granule deformation was a more important mechanism for further compaction at high relative density. Presumably, when the capacity for granule rearrangement has been exhausted and most of the intergranular spaces have been filled by fragmentation, deformation of the intragranular morphology is the only remaining compaction mechanism. It may be regarded as surprising that the slope of this part of the curve appeared to be around 2, suggesting that the nanostrain exceeded the macrostrain. Nevertheless, similar behaviour was also reported previously for sMCC [Laity et al. 2010a], which may be due to sudden collapse of the highly stressed intragranular morphology.

Mapping compaction behaviour:

Local variations in compaction behaviour, based on analysis of SAXS data collected at different locations across diametral sections of flat-faced, notched and bi-convex specimens compacted to P_{max} = 204 MPa, are shown in Figure 11. The black outlines represent the perimeters of the diametral sections used. It was not possible to analyse the SAXS data from a margin just inside the perimeter, due to contamination by 'spikes' of high intensity reflected off the edges and artefacts caused by severe differences in absorbance.

The colour-coded maps indicate the relative density, which was obtained from the Hermans parameter using the relationship described by Equation 16b. The superimposed white lines represent the principal compressive nanostrain, with magnitude given by Equation 17. In order to obtain the principle strain direction, the substitution:

$$\phi = \phi_{\mathrm{L}} + \psi \tag{18}$$

was made in Equation 15b, where ϕ_{L} represents the azimuthal angle in the 'laboratory frame' and searching for the value of ψ that maximised H.

Diametral sections from flat-faced cylindrical specimens showed the expected pattern of relative density variations, as demonstrated in Figure 11a. The largest variations occurred at the sides of the specimen, with the highest relative density (ρ_{rel} = 0·82 – 0·84) in the corners just below the upper (i.e. driven) face, the lowest (ρ_{rel} = 0·78 – 0·80) in the corners just above the lower (i.e. static) face and intermediate values (ρ_{rel} = 0·80 – 0·82) towards the centre of the diametral cross-section. To put these results in context, the average relative density, calculated from the mass and size of whole specimens compacted to P_{max} = 204 MPa, was 0·81. Moreover, based on the relationship between relative density and cohesive strength shown in Figure 4, these results suggested that the material in the bottom corners would have only around $^2/_3$ the cohesive strength of the upper corners.

This pattern of density variations was matched by the magnitude of the nanostrain, which ranged from 0·18 in the upper corners to 0·13 in the bottom corners. Over most of the cross-section, the principal strain direction was vertical (i.e. parallel to the bulk compaction direction). Small deviations (up to about 13°) were observed close to the sides, however, which may be ascribed to radial components of stress towards the die walls. These deviations were smaller than those observed previously in compacted sMCC (Laity and Cameron 2008, 2009, Laity et al. 2010a); this was also surprising in view of the high wall friction during ejection of the gMgSm specimens, suggesting considerable radial stress towards the die wall. It is possible, however, that larger deviations may have occurred within the unobservable margin, at the sides of the diametral cross-section.

Results from a notched specimen are presented in Figure 11b. The most obvious difference in compaction behaviour from the flat-faced specimen was the extreme variation around the debossed notch. A region of very high density (ρ_{rel} = 0·84 – 0·86, i.e. even higher than in the upper corners) was observed just below the notch, which extended towards the moderately high density region above the lower face. Conversely, very low density (ρ_{rel} = 0.71 – 0·74, i.e. even lower than in the bottom corners) was observed along the flanks of the notch. The magnitude of nanostrain also matched the density variations, while considerable local

variations were observed in the principal directions around the debossed notch, which suggested the forces 'spreading out' towards the sides of the specimens.

Results for a bi-convex specimen are shown in Figure 11c. Of the three shapes explored, this exhibited the greatest local variation in compaction behaviour, with a very dense belt (ρ_{rel} = 0·84 – 0·86) around the middle of specimen enclosing a very low density core (ρ_{rel} = 0·67 – 0·70). Based on the relationship shown in Figure 4, these results suggest that the core would have only around $^1/_3$ the cohesive strength of the surrounding belt. As before, the magnitude of the principal strain reflected the variations in relative density; however, the direction appeared to be significantly affected by the curvature of the upper and lower punches.

It may be noted that indications of local density variations from SAXS for the notched and bi-convex specimens were in agreement with (though much clearer than) the density variations indicated by XμT. The results for the compacted gMgSm specimens were also similar to those observed previously in corresponding sMCC specimens [Laity et al. 2010a, Laity 2014].

Estimation of compressive stress:

Local variations in compressive stress were estimated from SAXS data using Equation 16a; the results are presented as colour-coded maps in Figure 12.

The mean stress estimated from SAXS data across the diametral section for a flat-faced specimen (Figure 12a) was 250 MPa, which coincided reasonably well with the punch pressure used (204 MPa). Small local variations were evident (range ≈ 150 to 430 MPa), which corresponded to the local variations in relative density, as shown in Figure 11.

Much larger variations were observed within notched specimens (Figure 12b), with very high stress (> 2 GPa) estimated just below the notch and low stress (< 150 MPa) along the flanks. The changes in estimated stress with distance below the notch are shown in Figure 13a; the horizontal error bars (± 0·25 mm) represent the uncertainty in the distance from the bottom of the notch to the position where the SAXS data was collected; the vertical error bars (± 10 %) represent the uncertainty in estimating the stress from the SAXS data.

Compaction stresses around 250 – 300 MPa were indicated for different locations below the centres of the specimens, which were slightly larger than the average punch pressure actually used (204 MPa), but consistent with the region of moderately high density above the centre of the lower face. This effect may be attributed to the flow of granules being directed towards the centre of the specimen due to movement along the die wall being impeded by friction [Train 1956].

The stress appeared to increase towards the notch and values between 800 – 1000 MPa were indicated at 1 mm from the surface, which was considerably higher (i.e. over 4×) than the average punch pressure applied. As these estimates were only slightly above the calibration range used, they would appear to be quite reliable. Even higher stress (around 3·8 GPa) was indicated at 0·5 mm from the bottom of the notch; however, this involved considerable extrapolation from the calibration range and was less reliable.

It appeared that the stress values followed an exponential decay over distance below the notch (s) of the form:

$$P = B + C\exp(ks) \tag{19}$$

where B represents the plateau value at distance from the notch, C may be interpreted as the additional contact stress at the punch surface and k describes the rate of change. This is shown in Figure 13, along with the parameters used to fit the data. It may be noted that very similar behaviour was also reported recently for the compression of sMCC into debossed specimens, which was attributed to 'force-chains' and a largely 'columnar' transmission of force through the specimens [Laity 2014].

Large variations were also indicated within bi-convex specimens (Figure 12c), with a band of very high stress (from 500 to 1300 MPa) at the mid-line circumference, surrounding a central region of much lower stress (< 90 MPa). The changes with radial position are shown in Figure 13b. Again, it was found that an exponential relationship in the form of Equation 19 fitted the stress estimates well; extrapolation to 5 mm (corresponding to the outermost region, in contact with the die wall) suggested a maximal value around 1·64 GPa (i.e. 8× the average punch pressure used).

These variations in compressive stress could be important for several reasons. Firstly, excessive local contact stress may damage tooling surfaces, causing pitting and blunting the edges of embossed features (e.g. showing dose levels or logos on pharmaceutical tablets). Secondly, high compaction stresses may cause phase changes amongst susceptible materials. Thirdly, the close proximity of regions of high stress (resulting in high density with considerable elastic recovery during unloading) and lower stress (producing low density with poor cohesive strength) may account for the localised cracking observed around the debossed notches.

DISCUSSION AND CONCLUSIONS:

The present work was largely inspired by the potential use of granulated clays as pharmaceutical excipients. The compaction behaviour was studied, since compacted tablets represent popular, versatile and widely used formulations. Nevertheless, clay compaction also plays an important part in many natural and industrial processes; hence, the gMgSm used here may be regarded as a model system, giving the findings a wider significance in other fields.

A range of methods were used, including bulk force-displacement measurements, SEM, XRD and SAXS. Together, these revealed information ranging from the macroscopic behaviour of the powder bed to the response of the intragranular morphology at the nanometre scale.

Bulk measurements showed that gMgSm was somewhat harder to compact, compared with other common tabletting excipients such as sMCC, producing specimens with greater porosity (i.e. lower relative density) for a given maximum punch pressure. Nevertheless, the cohesive strengths of compacted gMgSm specimens appeared acceptable and were above those of sMCC specimens compacted to the same relative density (or porosity).

Somewhat surprisingly, the gMgSm exhibited significantly greater elastic recovery during unloading, compared with PGS and sMCC used in previous work. Measurements of constrained modulus for the gMgSm agreed well with previously published results for compacted clay minerals, but did not explain why it exhibited greater recovery than sMCC. The elasticity may also have been implicated in the high wall friction

and ejection forces observed with gMgSm specimens during compaction and the localised cracking around debossed features observed by XμT. It is likely that these aspects may be affected (ameliorated or exacerbated) by incorporating additional components (i.e. drugs and other excipients) in pharmaceutical formulations, which should be investigated in further work.

A large part of the work reported here was intended to demonstrate the capabilities of SAXS for investigating compaction behaviour. Applying SAXS to study powder compaction is a fairly recent development and the previous work used only polymeric materials (mainly PGS and sMCC). Nevertheless, as shown by the work reported here, SAXS was also particularly useful for investigating the compaction behaviour of gMgSm.

Prior to compaction, isotropic power-law scattering with roughly q^{-3} intensity dependence was observed for the gMgSm granules. This implied a fractal-like morphology, although it was not possible to deduce the precise structure. Compaction caused the 2D-SAXS patterns to become elongated, consistent with decreases in the characteristic lengths of the morphology in the compression direction. The magnitude of these changes in scattering increased reproducibly with compaction. Hence, empirical relationships with peak punch pressure and relative density could be found, which were subsequently used to investigate local variations in compaction behaviour within specimens.

Analysis of SAXS data from mapping experiments revealed the expected patterns of density variations in flat-faced cylindrical specimens due to friction against the die walls. Larger variations in density and principal strain (i.e. both magnitude and direction) were also observed around debossed notches and within bi-convex specimens. In particular, these observations suggested that the extensive cracking around debossed notches may have been caused by local variations in compaction, with high density regions undergoing considerable elastic recovery during unloading, in close proximity to low density regions of poor cohesive strength.

Moreover, analysis of the SAXS data provided estimates of the compaction stresses within the specimens. Although it is usual to discuss powder compaction in terms of average punch pressures, these results suggested that rather large local variations in stress had occurred when punches with curved surfaces or

embossed features were used. These stress variations may cause damage to tooling surfaces or phase changes in susceptible materials.

In spite of the obvious differences in chemical composition, the scattering data observed from gMgSm specimens showed distinct similarities to that observed previously from granules and compacted sMCC or PGS specimens. This can be explained by the SAXS originating from the pattern of electron density variations, which depended on the intragranular morphology. Hence, the similarities in scattering and changes following compaction between gMgSm, PGS and sMCC indicate common themes in the granular structures and responses – irrespective of the different chemical compositions. Indeed, the chemical composition was of secondary importance, although it clearly affected X-ray absorbance and may also control the more subtle details of compaction behaviour. It seems likely, therefore, that SAXS could also prove useful for investigating the compaction behaviour of other materials.

ACKNOWLEDGEMENTS:

The authors thank Dr Dasha Palmer of Lake Chemicals and Minerals Ltd. for the kind gift of granulated Veegum® (gMgSm). We would also like to thank the editor and the anonymous reviewers for their interesting and thought-provoking comments on this manuscript.

REFERENCES:

Aulton, M.E. 2007: Pharmaceutics: the design and manufacture of medicines. (3rd Edn. Churchill Livingstone, Elsevier).

Aguzzi, C. Cerezo, P. Viseras, C. Carmella, C. 2007: Use of clays as drug delivery systems: Possibilities and limitations. Appl. Clay Sci. 36: 22–36.

Asare-Addo, K. Laity, P.R. Ghori, M.U. Supuk, E. Conway, B.R. 2014: Pharmaceutical applications of smectite clays. 9th World Meeting on Pharmaceutics, Biopharmaceutics and Pharmaceutical Technology, Lisbon, Portugal (April 2014).

Baille, W. Tripathy, S. Schanz, T. 2010: Swelling pressures and one-dimensional compressibility behaviour of bentonite at large pressures. Appl. Clay. Sci.48; 324–333.

Baruchel, J. Buffière, J-Y. Maire, E.Merle, P. Peix, G. 2000, X-ray tomography in material science. (Hermes Science Publications, Paris.)

Beckett, C.T.S. Hall, M.R. Augarde, C.E. 2013: Macrostructural changes in compacted earthen construction materials under loading. Acta Geotechnica 8: 423–438.

Bergaya, F. Theng, B.K.G. Lagaly, G. (eds.) Handbook of clay science. 1st Edn. Elsevier Ltd. 2006.

Berisso, F.E. Schjønning, P. Keller, T. Lamandé, M. Etana, A. de Jonge, L.W. Iversen, B.V. Arvidsson, J. Forkman, J. 2012: Persistent effects of subsoil compaction on pore size distribution and gas transport in a loamy soil. Soil Tillage Resch. 122; 42–51.

Briscoe, B.J. Rough, S.L. 1998: The effects of wall friction in powder compaction. Coll. Surf. A. Physicochem. Eng. 137: 103-116.

Busignies, V. Leclerc, B. Porion, P. Evesque, P. Courraze, G. Tchoreloff, P. 2006: Quantitative measurements of localised density variations in cylindrical tablets using X-ray microtomography. Eur. J. Pharm. Biopharm. 64: 38-50.

Chipera, S.J. Bish, D.L. 2001: Baseline studies of the Clay Minerals Society Source Clays: powder X-ray diffraction analyses. Clay Clay Min. 49: 398-409.

Djemai, A. Sinka, I.C. 2006: NMR imaging of density distributions in tablets. Int. J. Pharm. 319: 55-62.

Feigin, L.A. Svergun, D.I. 1987: Structure analysis by small-angle X-ray and neutron scattering. Plenum Press, New York.

German, R.M. 2005: Powder metallurgy and particulate materials processing. (Metal Powder Industries Federation, Princeton, USA).

Hammond, C. 1997: The basics of crystallography and diffraction. International Union of Crystallography, Oxford University Press.

Han, L.H. Laity, P.R. Cameron, R.E. Elliott, J.A. 2011: Density and plastic strain evaluations using small-angle X-ray scattering and finite element simulations for powder compacts of complex shape. J. Mater. Sci. 46: 5977–5990.

Ito, H. 2006: Compaction properties of granular bentonites. Appl. Clay Sci.31; 47–55.

Kandeil, A. de Malherbe, MC. Critchley, S. Dokainish, M. 1997: The use of hardness in the study of compaction behaviour and die loading. Powder Technol. 17: 253-267.

Kim, S.W. Jung, H-D. Kang, M-H. Kim, H-E. Koh, Y-H. Estrin, Y. 2013: Fabrication of porous titanium scaffold with controlled porous structure and net-shape using magnesium as spacer. Mat. Sci. Eng. C 33: 2808–2815.

Kuklíc, P. 2011: Preconsolidation, structural strength of soil, and its effect on subsoil upper structure interaction. Eng. Struct, 33: 1195–1204.

Laity, P.R. Cameron, R.E. 2008: A small-angle X-ray scattering study of powder compaction. Powder Technol. 188: 119–127.

Laity, P.R. Cameron, R.E. 2009: A small-angle X-ray scattering study of local variations within powder compacts. Powder Technol. 192: 287–297.

Laity, P.R. Cameron, R.E. 2010a: Changes in small-angle X-ray scattering during powder compaction – an explanation based on granule deformation. Powder Technol. 198: 404–411.

Laity, P.R. Cameron, R.E. 2010b: Synchrotron X-ray microtomographic study of tablet swelling. Eur. J. Pharm. Biopharm. 75: 263–276.

Laity, P.R. Han, L.H. Elliott, J.A. Cameron, R.E. 2010a: Variations in compaction behaviour for tablets of different size and shape, revealed by small-angle X-ray scattering. J. Pharm. Sci. 99: 4380–4389.

Laity, P.R. Cassidy, A. Skepper, J. Jones, W. Cameron, R.E. 2010b: Investigation into the intragranular structures of microcrystalline cellulose and pre-gelatinised starch. Eur. J. Pharm. Biopharm. 74: 377–387.

Laity, P.R. 2014: Effects of punches with embossed features on compaction behaviour. Powder Technol. 254; 373–386.

Liddiard, P.D. 1984: Aluminium powder metallurgy in perspective. Powder Metall.27: 193-200.

Lide, D.R. (Ed.) 2002: CRC handbook of chemistry and physics, 82nd ed. (CRC Press, Boca Raton).

Macleod, H.M. Marshall, K. 1977: The determination of density distributions in ceramic compacts using autoradiography. Powder Technol. 16: 107-122.

Mc.Donald, S.A. Motazedian, F. Cocks, A.C.F. Withers, P.J. 2009: Shear cracking in an Al powder compact studied by X-ray microtomography. Mat. Sci. Eng. A 508: 64–70.

Mondol, N.H. Bjørlykke, K. Jahren, J. Høeg, K. 2007: Experimental mechanical compaction of clay mineral aggregates - changes in physical properties of mudstones during burial. Marine Petroleum Geol. 24; 289–311.

Morel, J.C. Pkla, A. Walker, P. 2007: Compressive strength testing of compressed earth blocks. Constr. Building Mats. 21: 303–309.

Moyano, B. Spikes, K.T. Johansen, T.A. Mondol, N.H. 2012: Modeling compaction effects on the elastic properties of clay-water composites. Geophysics 77: D171-D183.

Murray, H.H. 2000: Traditional and new applications for kaolin, smectite, and palygorskite: a general overview. Appl. Clay Sci. 17: 207–221.

Nebgen, G. Gross, D. Lehmann, V. Muller, F. 1995: ^{1}H-NMR microscopy of tablets. J. Pharm. Sci. 84: 283–291.

Oh, C. Sorensen, C.M. 1999: Scaling approach for the structure factor of a generalized system of scatterers. J. Nanopart. Resch. 1: 369-377.

Pizette, P. Martin, C.L. Delette, G. Sans, F. Geneves, T. 2013: Green strength of binder-free ceramics. J. Eur. Ceram. Soc. 33: 975–984.

Pongjanyakul, T. Rojtanatanya, S. 2012: Use of propranolol-magnesium aluminium silicate intercalated complexes as drug reservoirs in polymeric matrix tablets. Ind. J. Pharm. Sci. 74: 292-301.

Prakash, K. Sridharan, A. Prasanna, H.S. 2013: Compaction induced yield stress. Geotech. Geol. Eng. DOI 10.1007/s10706-013-9715-6.

Rahaman, M.N. 2003: Ceramic processing and sintering. Marcel Dekker Inc. New York.

Roe, R-J. 2000 Methods of X-ray and neutron scattering in polymer science. Oxford University Press, New York.

Romero, E. 2013: A microstructural insight into compacted clayey soils and their hydraulic properties. Eng. Geol. 165: 3–19.

Schmidt, PW. 1991: Small-angle scattering studies of disordered, porous and fractal systems. J. Appl. Cryst. 24; 414–435.

Sinka, IC. Motazedian, F. Cocks, ACF. Pitt. KG. 2009: The effect of processing parameters on pharmaceutical tablet properties. Powder Technol. 189: 276-284.

Sinka, I.C. Burch, S.F. Tweed, J.H. Cunningham, J.C. 2004: Measurement of density variations in tablets using X-ray computed tomography. Int. J. Pharm. 271: 215-224.

Sorensen, C.M. 2001: Light scattering by fractal aggregates: a review. Aerosol Sci. Technol. 35: 648–687.

Stock, S.R. 1999: X-ray microtomography of materials. Int. Mat. Rev.44: 141-164.

Sun, C. 2004: A novel method for deriving true density of pharmaceutical solids including hydrates and water-containing powders. J. Pharm. Sci. 93: 646–653.

Tien, Y.M. Wu, P.L. Chuang, W.S. Wu, L.H. 2004: Micromechanical model for compaction characteristics of bentonite–sand mixtures. Appl. Clay Sci. 26: 489–498.

Train, D. 1956: An investigation into the compaction of powders, J. Pharm. Pharmacol. 8: 745–761.

Vanorio, T. Prasad, M. Nur, A. 2003: Elastic properties of dry clay mineral aggregates, suspensions and sandstones. Geophys. J. Int. 155: 319-326.

Villamizar, M.C. Araque, V. C. Reyes, C.A.R. Silva, R.S. 2012: Effect of the addition of coal-ash and cassava peels on the engineering properties of compressed earth blocks. Constr. Building Mats. 36: 276–286.

Villar, M.V. Lloret, A. 2008: Influence of dry density and water content on the swelling of a compacted bentonite. Appl. Clay Sci. 39; 38–49.

Villar, M.V. Gómez-Espina, R. Gutiérrez-Nebot, L. 2012: Basal spacings of smectite in compacted bentonite. Appl. Clay Sci. 65-66; 95–105.

Wu, C-Y. Hancock, B.C. Mills, A. Bentham, A.C. Best, S.M. Elliott, J.A. 2008: Numerical and experimental investigation of capping mechanisms during pharmaceutical tablet compaction. Powder Technol. 181; 121–129.

Ye, W.M. Zhang, Y.W. Chen, B. Zheng, Z.J. Chen, Y.G. Cui, Y.J. 2012: Investigation on compression behaviour of highly compacted GMZ01 bentonite with suction and temperature control. Nucl. Eng. Des. 252; 11–18.

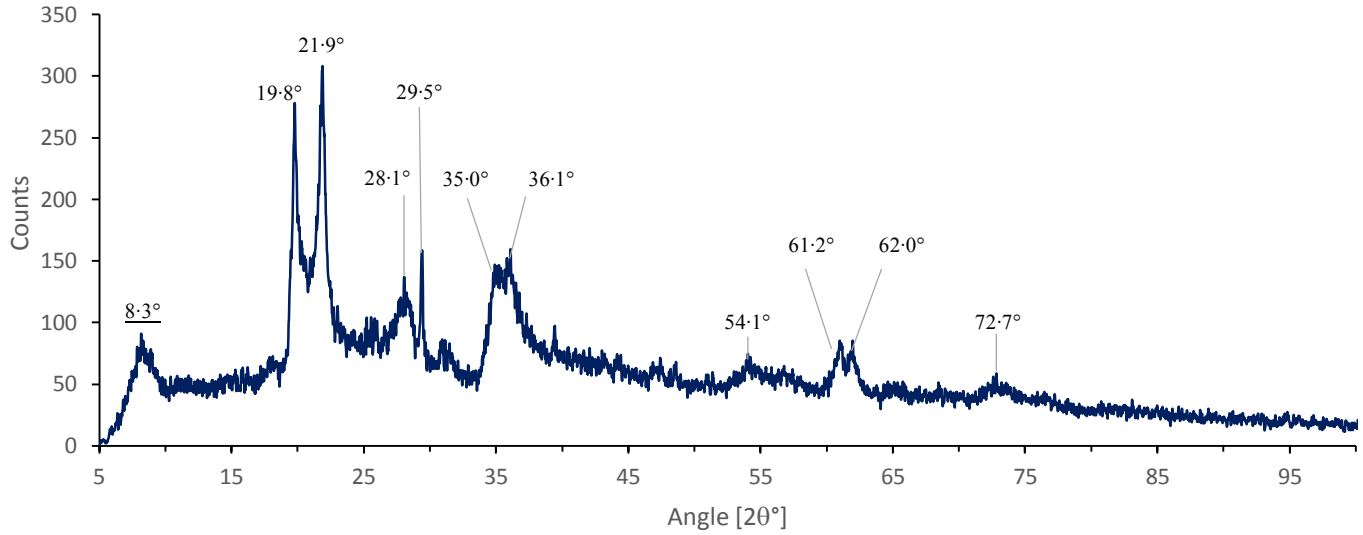

Figure 1: XRD pattern measured for randomly oriented, uncompacted gMgSm powder. The Bragg angles of the main reflections are indicated on the figure, with the value for the basal reflection underlined.

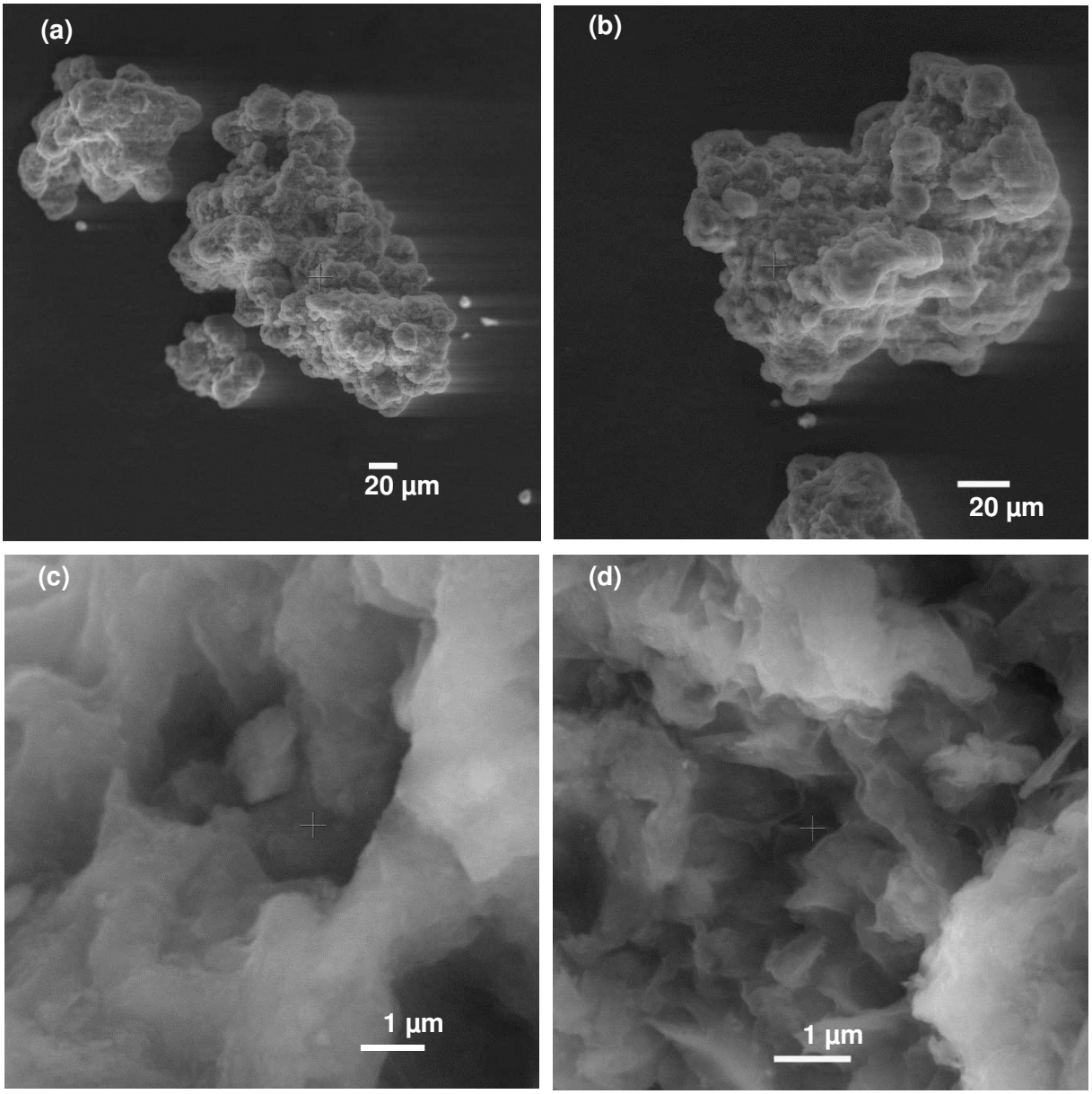

Figure 2: SEM images of gMgSm: (a) and (b) at low magnification, showing shapes of typical granules; (c) and (d): at higher magnification, showing structural details.

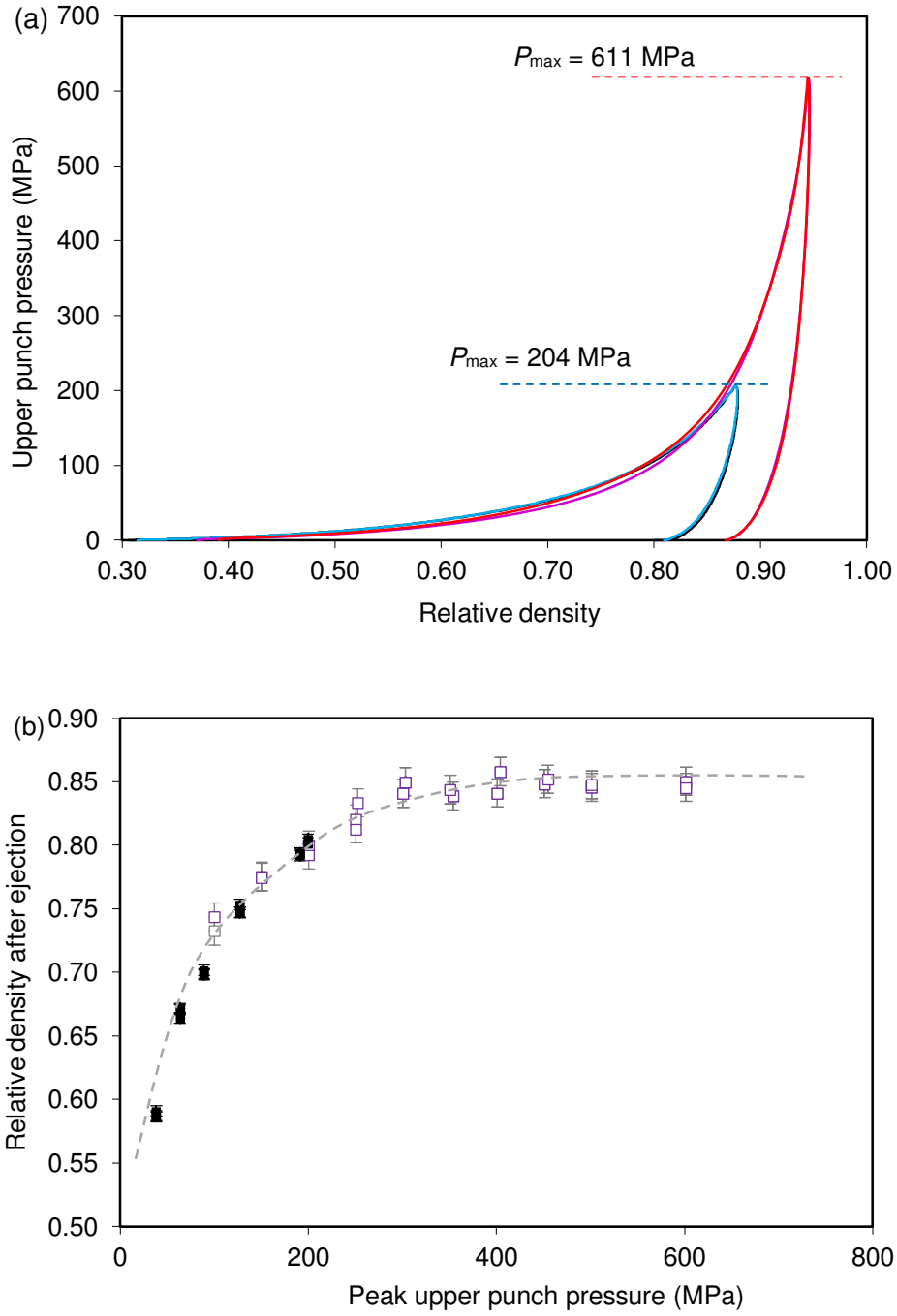

Figure 3: Compaction behaviour of gMgSm:(a) typical plots of upper punch pressure vs. relative density, measured during compaction experiments to 204 MPa and 611 MPa peak pressure (both in duplicate; plots also discriminated by colour in on line version); (b) relationship between peak upper punch pressure and relative densities of the ejected specimens prepared with R = *5·0 mm (filled* symbols) and R = *2·5* mm (open symbols); the dashed grey line merely provides a guide for the eye.

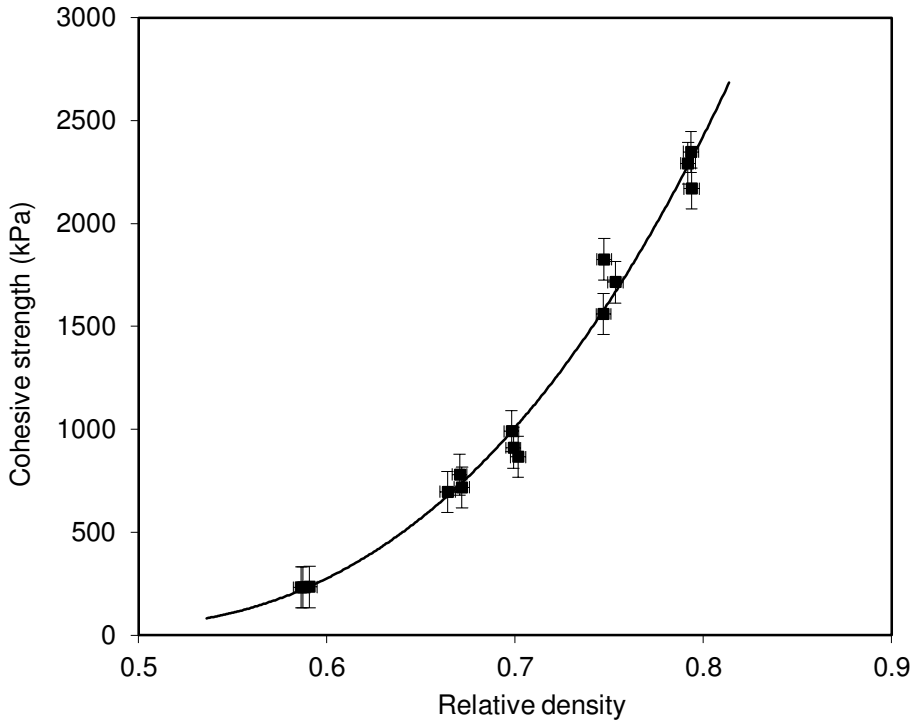

Figure 4: Cohesive strength of compacted gMgSm specimens in relation to relative density.

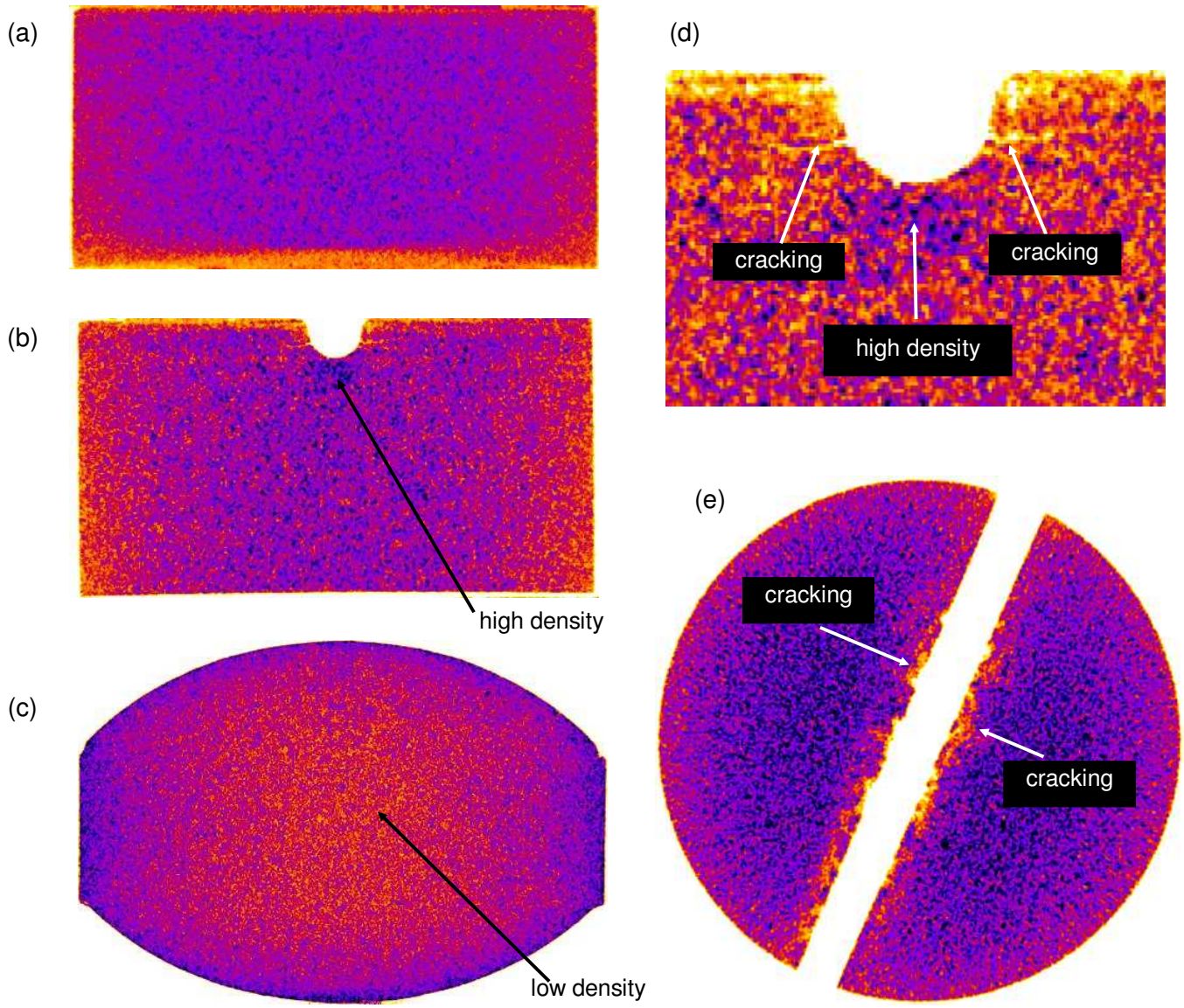

Figure 5: X-ray microtomographic images of compacted gMgSm specimens (to 204 MPa); (a) – (c) sagittal sections showing the profiles of flat-faced, notched and biconvex specimens; (d) detail from sagittal section showing density variations and cracking around a debossed notch; (e) coronal section showing cracking *along a debossed notch. In each case, the diameter of the compacted specimen was 10·0 mm.* False colour (on-line version) has been applied to aid viewing, with blue indicating higher density.

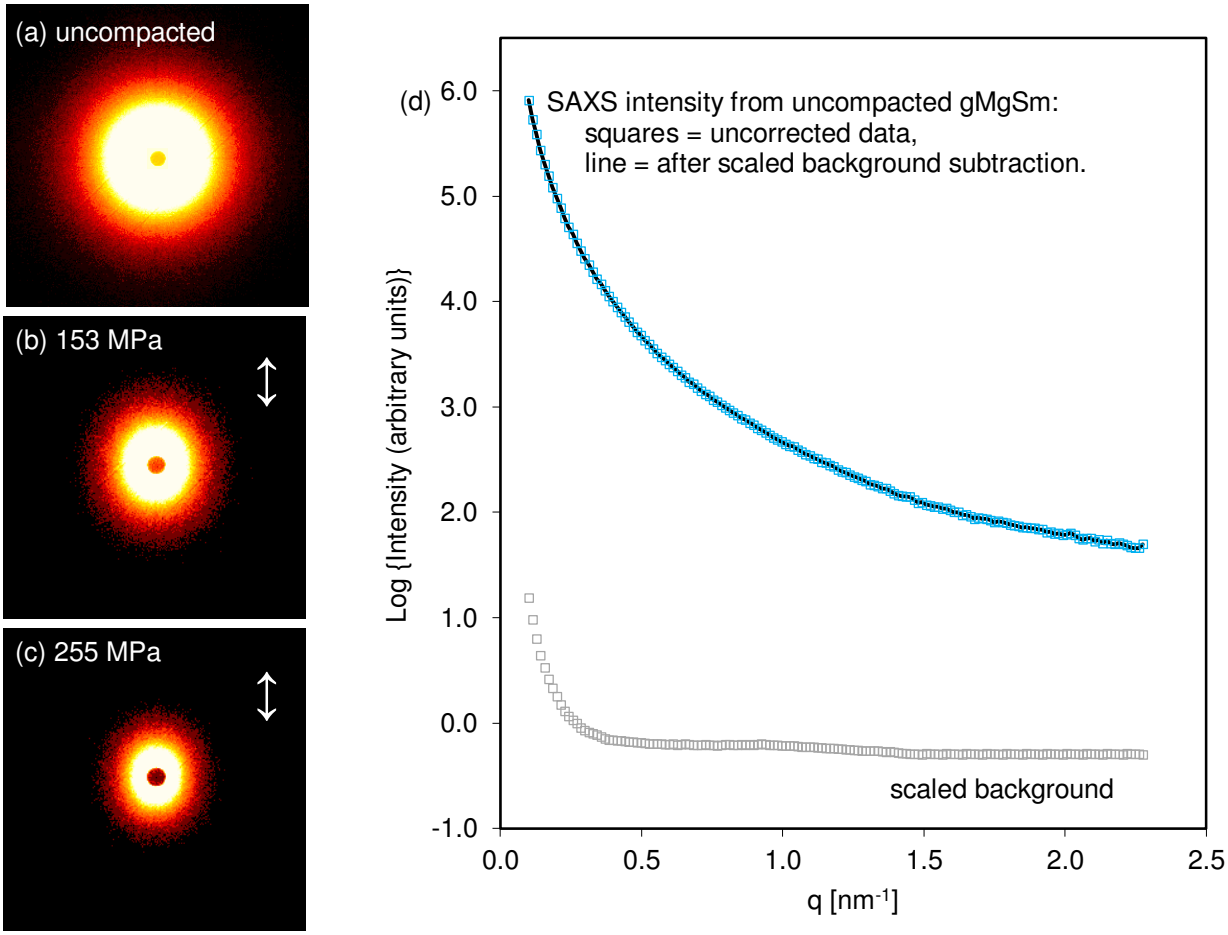

Figure 6: Typical SAXS data for gMgSm: (a - c) 2D-SAXS patterns for uncompacted powder and specimens compacted to 153 or 255 MPa (the dark spots in the centre of the SAXS patterns are the shadows of the beam-stop, the double-headed arrows indicate the compaction direction); (d) 1D-SAXS intensity curves from radial scans through 2D-SAXS data for uncompacted gMgSm and background from empty camera, scaled for sample transmission.

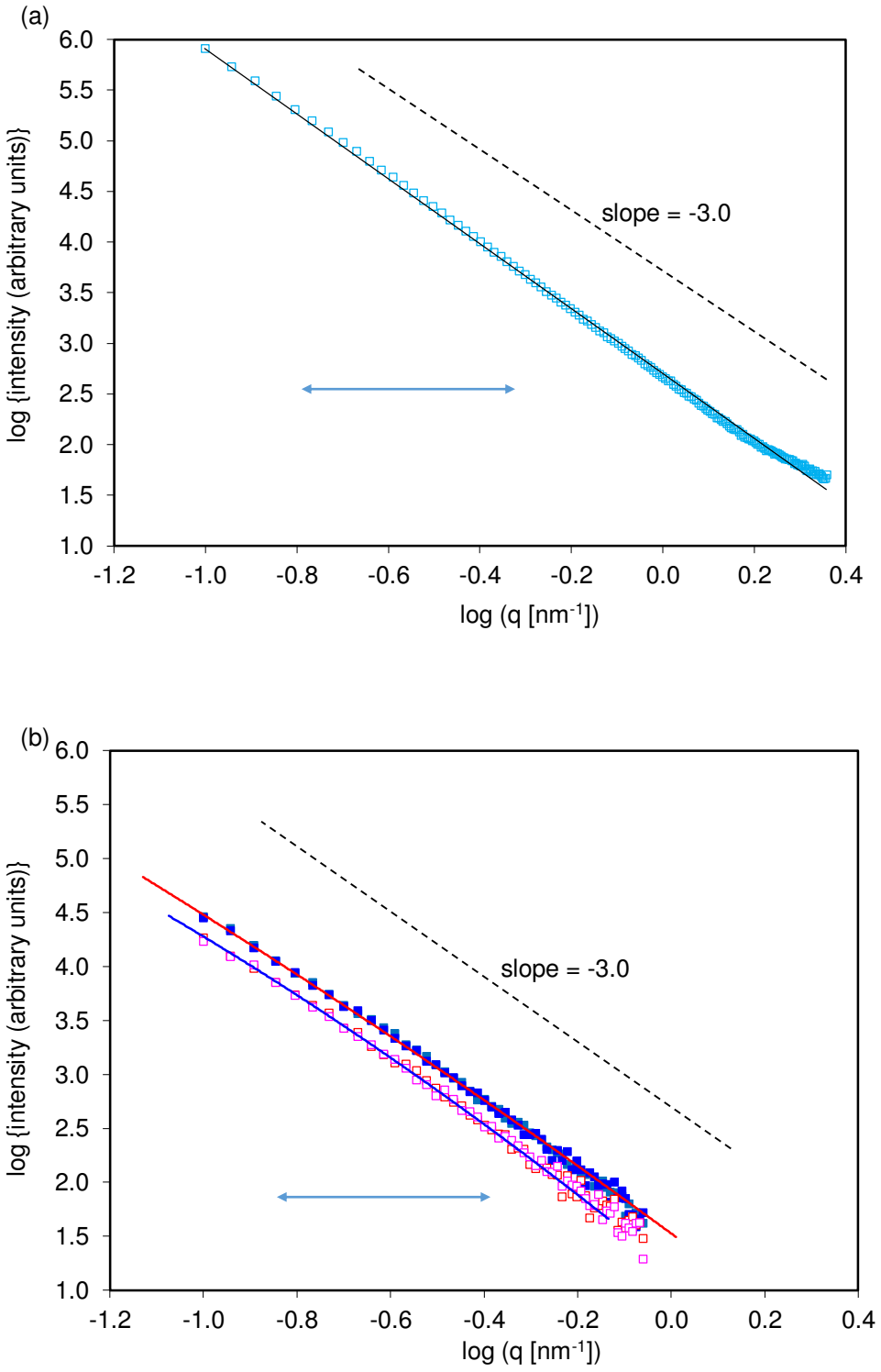

Figure 7: Radial intensity scans through typical SAXS data for gMgSm: (a) uncompacted powder; (b) after compaction to 255 MPa. In both cases, the units of q were nm^{-1}. The continuous lines in (b) represent the *best fits through the data measured in the 'other' direction and scaled according to Equation* 12, *using* α = 2·92 and b = 0·847. For comparison. the dashed lines have a slope of -3·0. The double-headed arrows indicate the q-range used to obtain the azimuthal intensity variations.

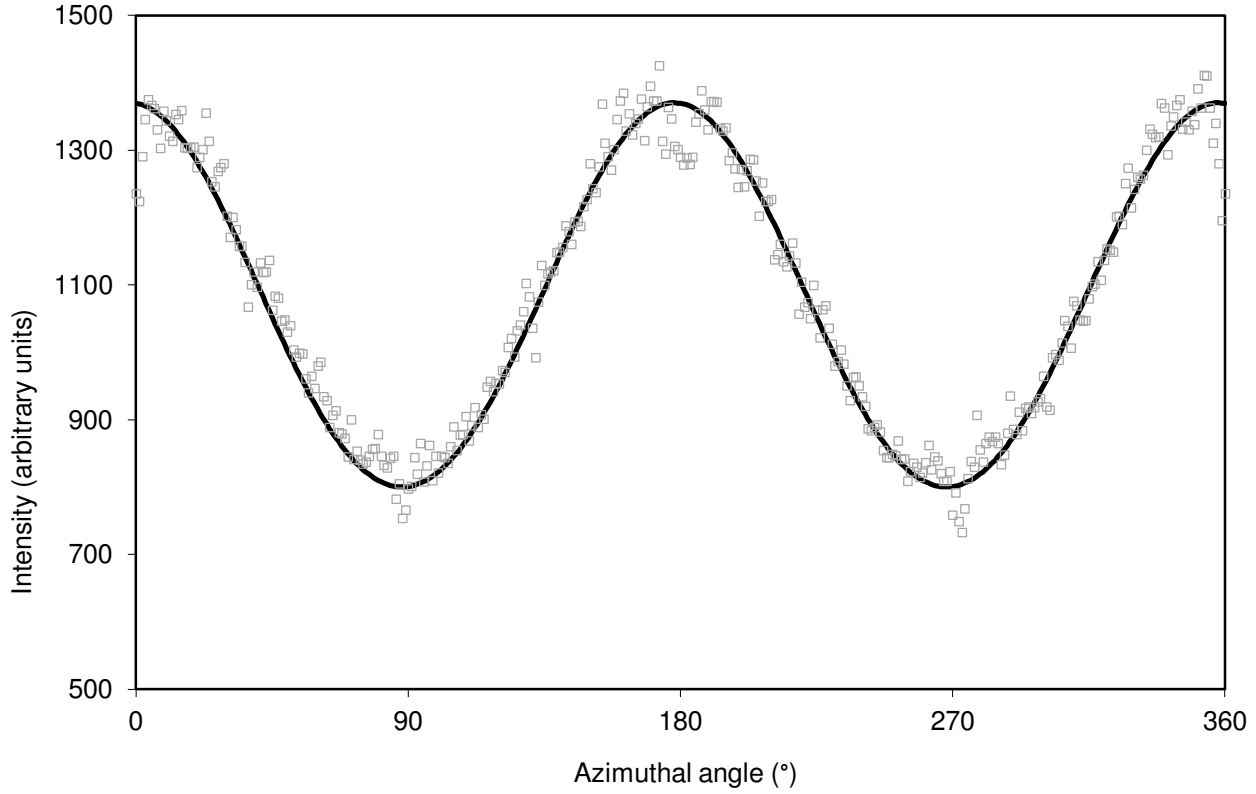

Figure 8: Azimuthal intensity scans through typical SAXS data for gMgSm compacted to 255 MPa. The intensity was obtained by integration over q = *0·14 to 0·43* nm^{-1}(corresponding to the scattering angle from *0·2 to 0·6°). T*he continuous line represents the best fit to the data using the model described by Equation 14.

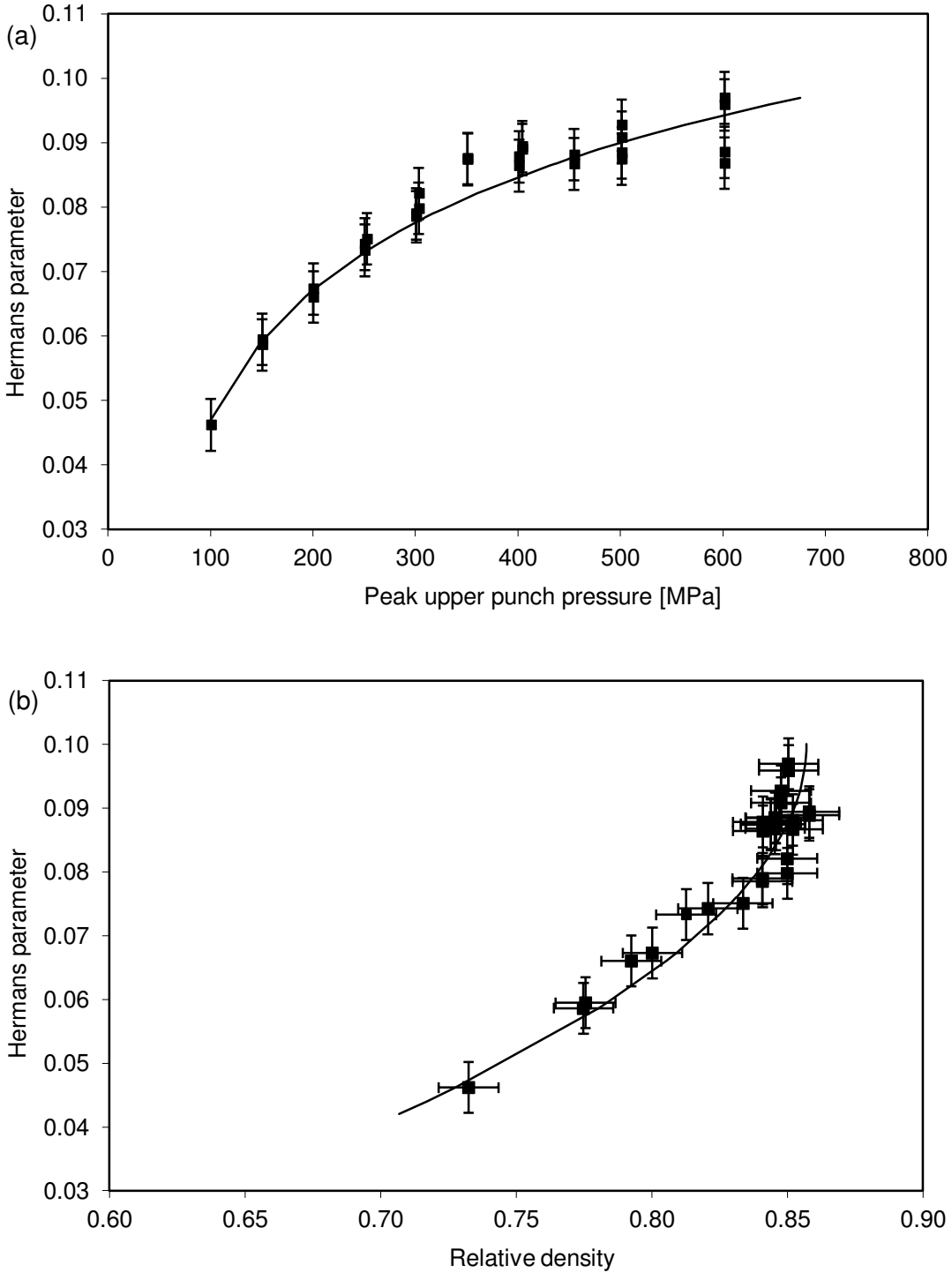

Figure 9: Changes in azimuthal variation, quantified as the Hermans parameter, with respect to: (a) peak upper punch pressure, (b) relative density. The continuous lines show the best fits achieved using the models described by Equations 16a and 16b.

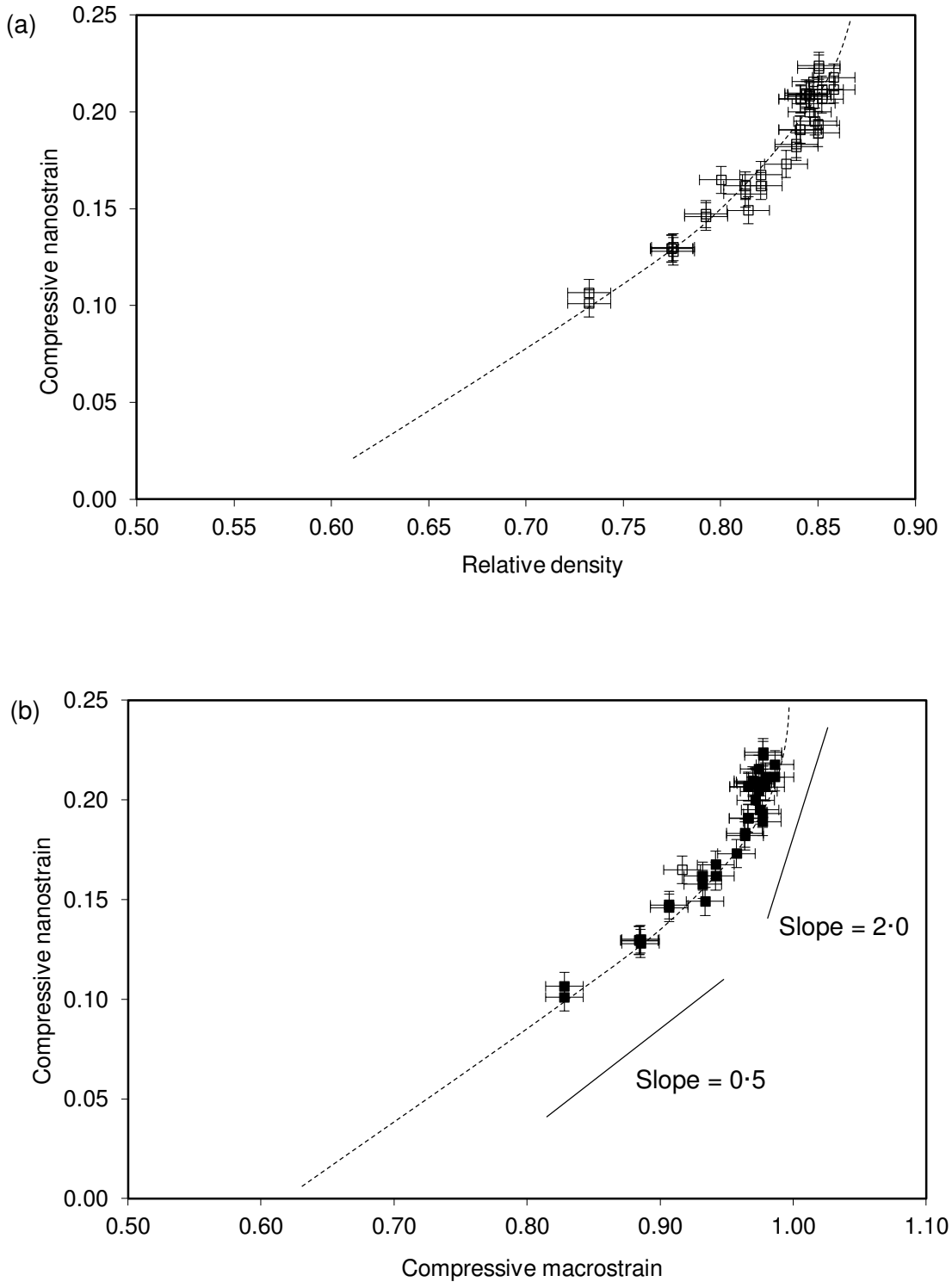

Figure 10*: Changes in the compressive 'nanostrain' of the intragranular morphology, estimated from SAXS* data, with respect to: (a) mean relative density of the compact, (b) compressive macroscopic strain of the powder bed. The dashed lines merely provide a guide for the eye.

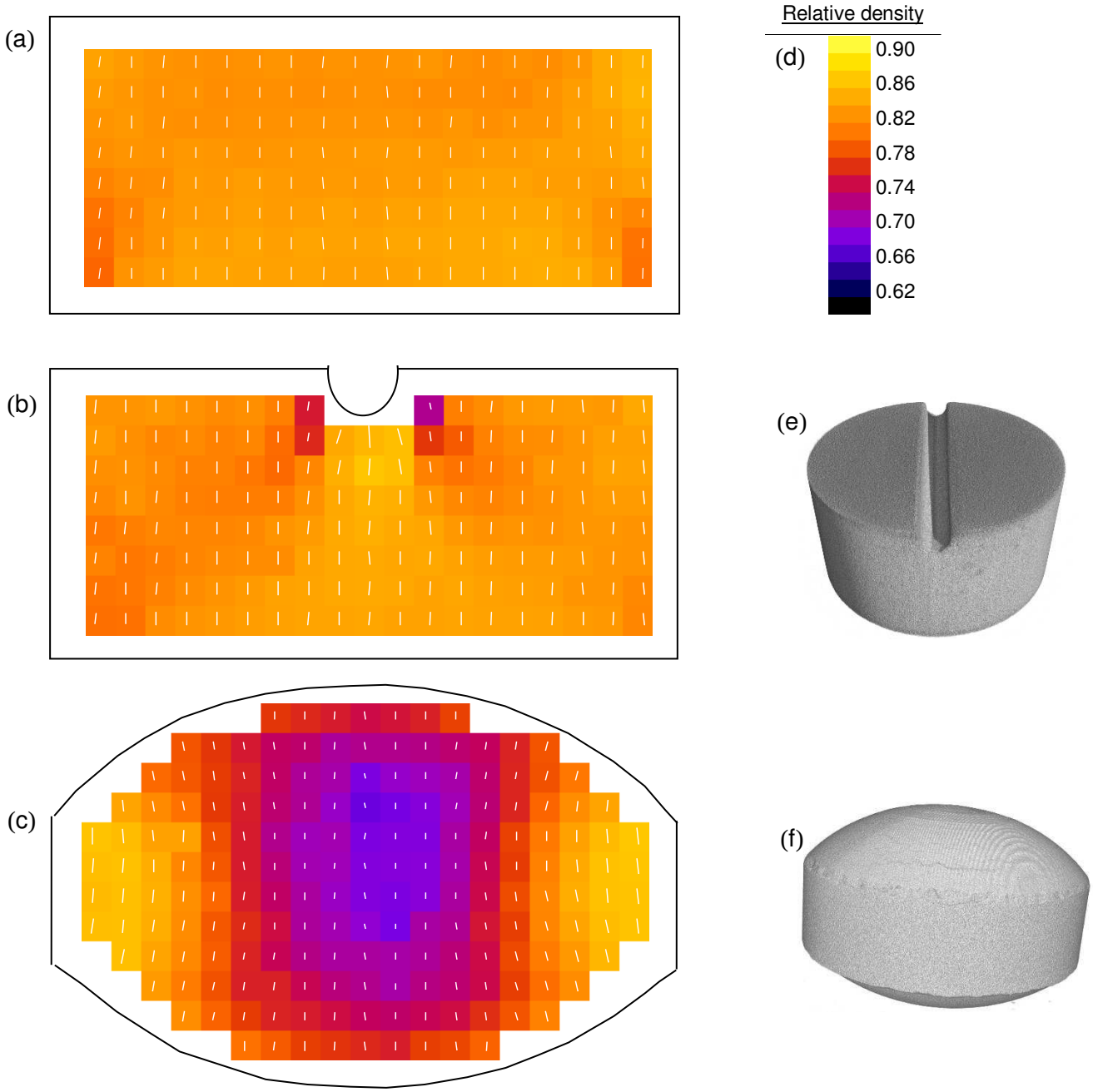

Figure 11: Colour-coded maps showing relative density variations from analysis of SAXS data, across diametral sections of (a) flat-faced, (b) notched and (c) bi-convex specimens of compacted gMgSm (P_{max} = 204 MPa). The relative densities are represented using the scale shown in (d). The black lines in a – c represent the perimeters of the diametral sections, the superimposed white lines show the relative magnitude and direction of the compressive strain experienced by the nanometre-scale morphology. To assist in relating the diametral sections to the specimens analysed, thumbnail images of the notched and biconvex compacts (surface-rendered from XμT data) are shown in (e) and (f).

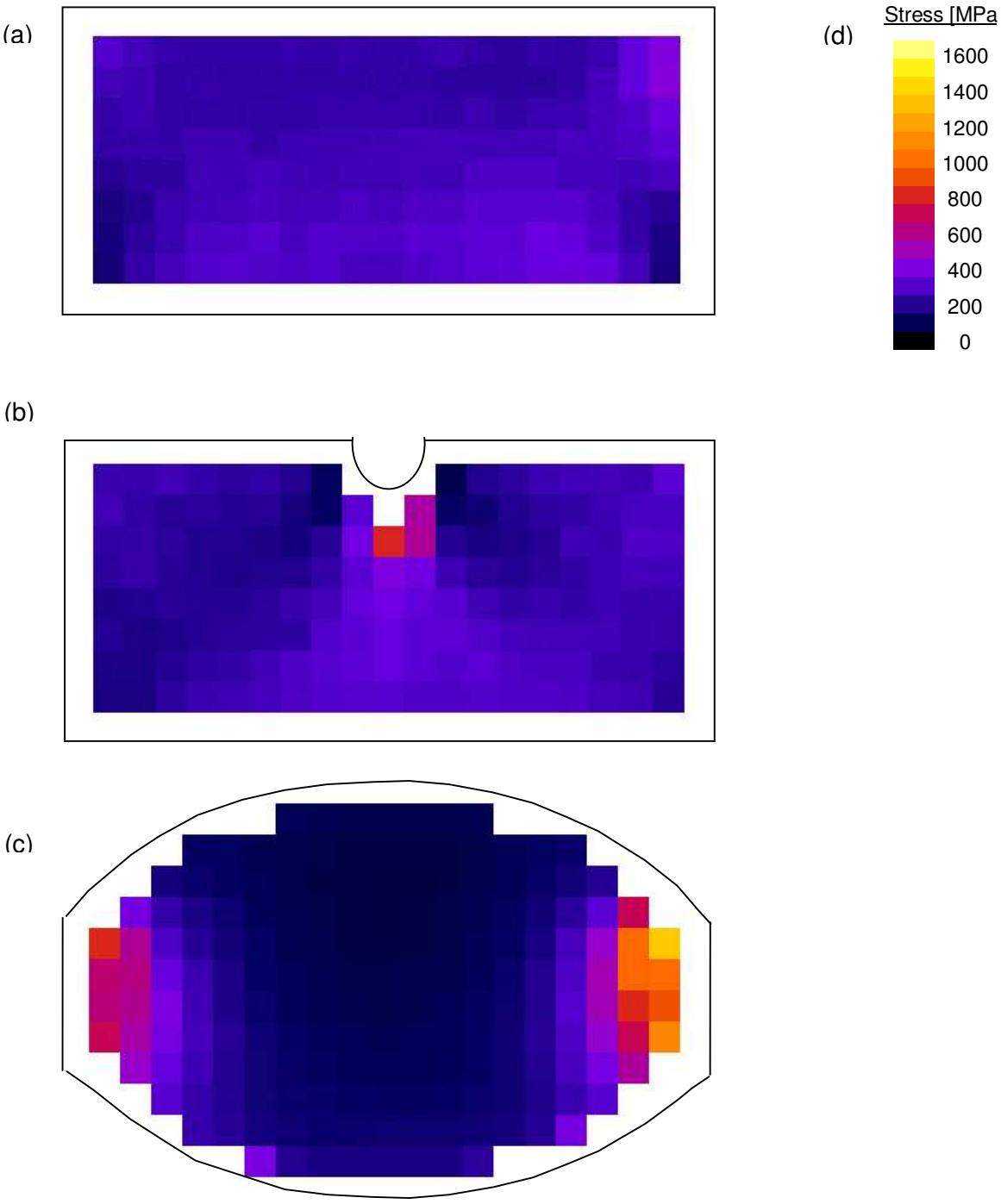

Figure 12: Colour-coded maps showing local compressive stress variations estimated from analysis of SAXS data, across diametral sections of (a) flat-faced, (b) notched and (c) bi-convex specimens of compacted gMgSm (P_{max} = 204 MPa) from analysis of SAXS data, represented using the scale (d). The black lines represent the perimeters of the diametral sections, as in figure 11.

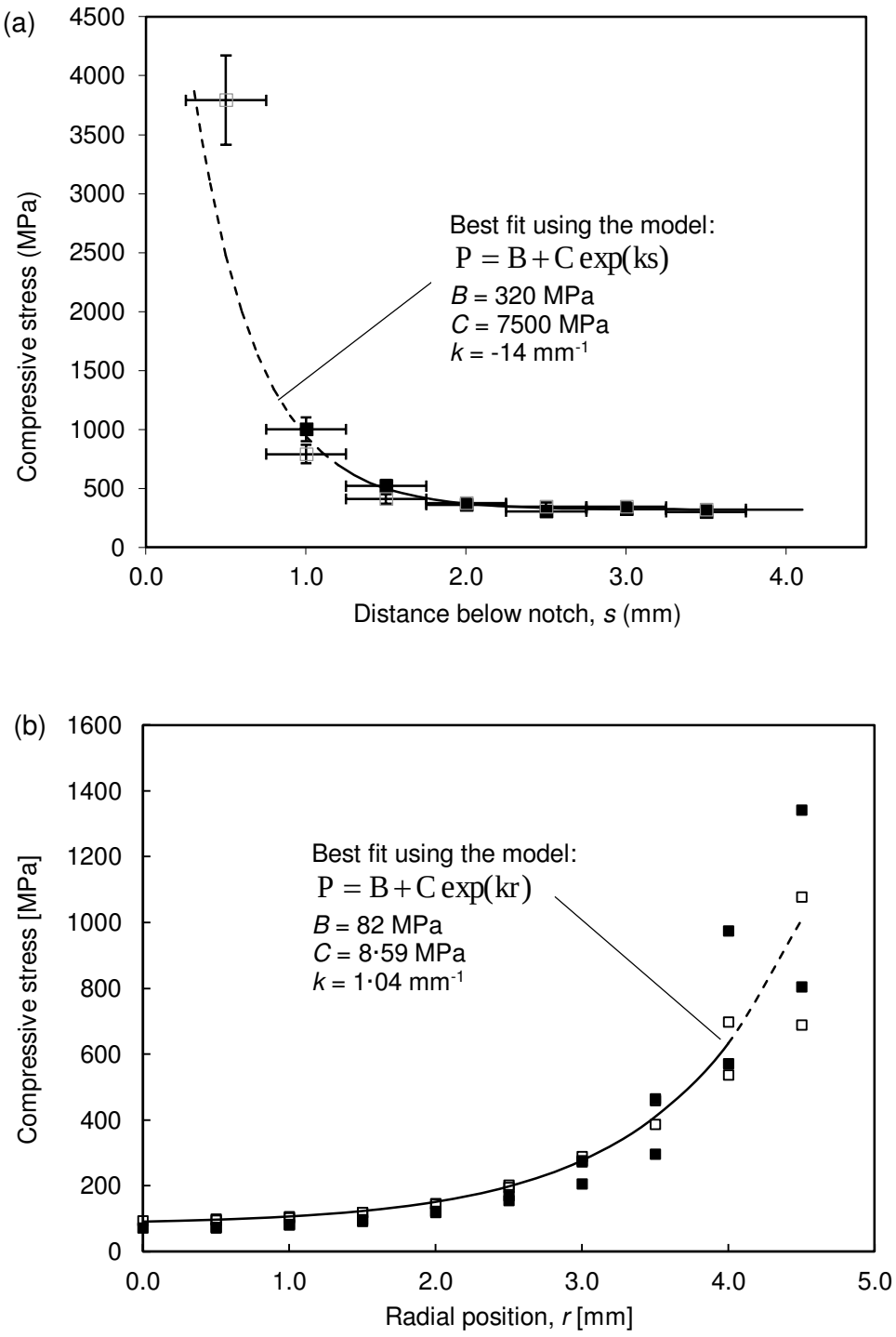

Figure 13: Estimated compressive stress from SAXS data using Equation 16a, for compacted gMgSm specimens prepared at 204 MPa average punch pressure: (a) for locations directly below debossed notches; (b) across the mid-line of bi-convex specimens. The curves represent the best fits through the data, as described by the equations with the values shown; the dashed sections represent extrapolation beyond the calibration range.